



City Research Online

City, University of London Institutional Repository

Citation: Tsantani, M., Kriegeskorte, N., Storrs, K., Williams, A. L., McGettigan, C. & Garrido, L. (2021). FFA and OFA encode distinct types of face identity information. *The Journal of Neuroscience*, 41(9), pp. 1952-1969. doi: 10.1523/jneurosci.1449-20.2020

This is the accepted version of the paper.

This version of the publication may differ from the final published version.

Permanent repository link: <https://openaccess.city.ac.uk/id/eprint/25458/>

Link to published version: <https://doi.org/10.1523/jneurosci.1449-20.2020>

Copyright: City Research Online aims to make research outputs of City, University of London available to a wider audience. Copyright and Moral Rights remain with the author(s) and/or copyright holders. URLs from City Research Online may be freely distributed and linked to.

Reuse: Copies of full items can be used for personal research or study, educational, or not-for-profit purposes without prior permission or charge. Provided that the authors, title and full bibliographic details are credited, a hyperlink and/or URL is given for the original metadata page and the content is not changed in any way.

FFA and OFA encode distinct types of face identity information

Abbreviated title: Face identity encoding in FFA and OFA

Maria Tsantani (maria.tsantani@gmail.com)¹

Division of Psychology, Department of Life Sciences, Brunel University London, Uxbridge UB8 3PH, UK

Nikolaus Kriegeskorte (nk2765@columbia.edu)

Zuckerman Mind Brain Behavior Institute, Columbia University, New York, NY 10027, USA

Katherine Storrs (katherine.storrs@gmail.com)

Department of Experimental Psychology, Justus Liebig University, 35390 Giessen, Germany

Adrian Lloyd Williams (adrian.williams@brunel.ac.uk)

Division of Psychology, Department of Life Sciences, Brunel University London, Uxbridge UB8 3PH, UK

Carolyn McGettigan (c.mcgettigan@ucl.ac.uk)

Speech Hearing and Phonetic Sciences, University College London, London WC1N 1PF, UK

Lúcia Garrido (lucia.garrido@city.ac.uk)¹

Division of Psychology, Department of Life Sciences, Brunel University London, Uxbridge UB8 3PH, UK

¹Corresponding authors

[Figures: 7](#)

[Tables: 2](#)

Conflict of interest

The authors declare no competing financial interests.

Acknowledgements

This work was supported by a research grant by the Leverhulme Trust (RPG-2014-392) to LG, NK, and CM. We thank Tiana Rakotonombana, Roxanne Zamyadi, Rasanat Nawaz, and Natasha Baxter for help with stimuli preparation and with testing.

Current affiliations: Maria Tsantani: Department of Psychological Sciences, Birkbeck, University of London, London WC1E 7HX, UK; Lúcia Garrido: Department of Psychology, City, University of London, London EC1V 0HB, UK

Abstract

Faces of different people elicit distinct functional MRI (fMRI) patterns in several face-selective regions of the human brain. Here we used representational similarity analysis to investigate what type of identity-distinguishing information is encoded in three face-selective regions: fusiform face area (FFA), occipital face area (OFA), and posterior superior temporal sulcus (pSTS). In a sample of 30 human participants (22 females, 8 males), we used fMRI to measure brain activity patterns elicited by naturalistic videos of famous face identities, and compared their representational distances in each region with models of the differences between identities. We built diverse candidate models, ranging from low-level image-computable properties (pixel-wise, GIST, and Gabor-jet dissimilarities), through higher-level image-computable descriptions (OpenFace deep neural network, trained to cluster faces by identity), to complex human-rated properties (perceived similarity, social traits, and gender). We found marked differences in the information represented by the FFA and OFA. Dissimilarities between face-identities in FFA were accounted for by differences in perceived similarity, social traits, gender, and by the OpenFace network. In contrast, representational distances in OFA were mainly driven by differences in low-level image-based properties (pixel-wise and Gabor-jet dissimilarities). Our results suggest that, although FFA and OFA can both discriminate between identities, the FFA representation is further removed from the image, encoding higher-level perceptual and social face information.

Keywords: representational similarity analysis; face identity; FFA; OFA

Significance statement

Recent studies using functional magnetic resonance imaging (fMRI) have shown that several face-responsive brain regions can distinguish between different face identities. It is however unclear whether these different face-responsive regions distinguish between identities in similar or different ways. We used representational similarity analysis to investigate the computations within three brain regions in response to naturalistically varying videos of face identities. Our results revealed that two regions, the fusiform face area (FFA) and the occipital face area (OFA), encode distinct identity information about faces. Although identity can be decoded from both regions, identity representations in FFA primarily contained information about social traits, gender, and high-level visual features, whereas OFA primarily represented lower-level image features.

The human brain contains several face-selective regions that consistently respond more to faces than other visual stimuli (Kanwisher et al., 1997; Pitcher et al., 2011; Rossion et al. 2012; Khuvis et al., 2018; Axelrod et al., 2019). Functional magnetic resonance imaging (fMRI) has revealed that some of these regions represent different face identities with distinct brain patterns. Specifically, studies using fMRI multivariate pattern analysis have shown that face identities can be distinguished based on their elicited response patterns in the fusiform face area (FFA), occipital face area (OFA), posterior superior temporal sulcus (pSTS), and anterior inferior temporal lobe (Nestor et al. 2011; Verosky et al., 2013; Goesaert & Op de Beeck, 2013; Anzellotti et al., 2014; Axelrod & Yovel, 2015; Zhang et al., 2016; Anzellotti & Caramazza, 2017; Guntupalli et al., 2017; Visconti di Oleggio Castello et al., 2017; Tsantani et al., 2019; see also Davidesco et al. (2014), Ghuman et al. (2014), and Khuvis et al. (2018) for results using intracranial electroencephalography, iEEG). But do these regions represent the same information and, if not, what information is explicitly encoded in each of these face-selective regions?

Behaviourally, we distinguish between different faces using the surface appearance of the face, the shape of face features, and their spacing or configuration (e.g. Rhodes, 1988; Calder et al., 2001; Yovel & Duchaine, 2006; Russell & Sinha, 2007; Russell et al., 2007; Tardif et al., 2019). In particular, Abudarham and Yovel (2016) recently showed that features such as lip thickness, hair colour, eye colour, eye shape, and eyebrow thickness were crucial in distinguishing between individuals (see also Abudarham et al., 2019). Additionally, we perceive a vast amount of socially-relevant information from faces that can be used to distinguish between different individuals, such as gender, age, ethnicity, social traits (Oosterhof & Todorov, 2008; Sutherland et al. 2013), and even relationships and social network position (Parkinson et al., 2014; 2017). Therefore, if the response patterns in a certain brain region distinguish between two individuals, that region could be representing any one—or a combination of —these dimensions.

Like several other studies (see above), Goesaert and Op de Beeck (2013) demonstrated that the FFA, OFA, and a face-selective region in the anterior inferior temporal lobe could all decode between different face identities based on fMRI response patterns. Importantly, the authors further tested what type of face information was *encoded* in these different regions. The authors found that all three regions could distinguish between faces using both configural and featural face information, and therefore all regions seemed to represent similar information. Goesaert and Op de Beeck (2013) also showed that representational distances between different faces in face-selective regions did not correlate with low-level pixel-based information. This study however, used one single image for each person's face, making it difficult to disentangle whether representations in a certain brain region are related to identity *per se* or related to the specific images used.

To determine whether brain response patterns represent face identity *per se*, it is necessary to show that patterns generalise across different images of the same person's face, in addition to distinguishing that person's face from the faces of other people. Anzellotti et al (2014) showed that classifiers trained to decode face identities in the FFA, OFA, anterior temporal lobe, and pSTS (later analysed in Anzellotti and Caramazza, 2017) could also decode the same faces from novel viewpoints. Guntupalli et al (2017) additionally showed a hierarchical organisation of the functions of face-selective regions,

with the OFA decoding viewpoint of face independently of the face identity, the anterior inferior temporal lobe (and a region in the inferior frontal cortex) decoding face identity independently of the viewpoint, and the FFA decoding both viewpoint and identity information (see also Dubois et al., 2015). Extending these findings and using iEEG in epilepsy patients, Ghuman et al (2014) showed invariant decoding in the FFA across different facial expressions. In contrast, Grossman et al (2019) have recently shown that representational distances between different face identities (computed from brain response patterns recorded from implanted electrodes) were very similar across the OFA and the FFA (in the left hemisphere). Crucially, the representational geometries in both regions were associated with differences in image-level descriptions computed from a deep neural network (VGG-Face), which were not generalisable across different viewpoints of the same person's face. These results thus suggest that the OFA and FFA both represent complex configurations of image-based information and not face identity *per se*.

Also using iEEG, Davidesco et al. (2014) further showed that representational distances between face images in the FFA (and to a lesser extent in the OFA) were associated with perceived similarity and characteristics of facial features (such as face area and mouth width), but not with low-level features related to pixel-based information (see also Ghuman et al, 2014). Some fMRI studies have shown that even lower-level stimulus-based properties of face images, such as those computed by Gabor filters, explain significant variance in the representational geometries in the FFA (Carlin & Kriegeskorte, 2017) as well as OFA and pSTS (Weibert et al., 2018). On the other hand, other studies have shown that more high-level information, such as biographical information and social context, affects the similarity of response patterns to different faces in the FFA (Verosky et al., 2013; Collins et al., 2016).

There is thus mixed evidence regarding whether different face-selective regions rely on similar or distinct information to distinguish between face identities, and what type of information may be encoded in different regions. In the present study, we used representational similarity analysis (RSA) (Kriegeskorte et al., 2008a; 2008b) to investigate what type of identity-distinguishing information is encoded in different face-selective regions. In our previous work (Tsantani et al., 2019), we showed that famous face-identities could be distinguished in the right FFA, OFA, and pSTS based on their elicited fMRI response patterns. Here, for the same set of famous identities and using the same data as in Tsantani et al (2019), we compared the representational distances between identity-elicited fMRI patterns in these regions with diverse candidate models of face properties that could potentially be used to distinguish between identities.

Importantly, we used multiple naturalistically varying videos for each identity that varied freely in terms of viewpoint, lighting, head motion, and general appearance. In addition, our representational distances were cross-validated across different videos, in order to deconfound identity from incidental image properties. By using a large, diverse set of candidate models, based on image properties of the stimuli (*image-computable models*) and on human-rated properties (*perceived-property models*), we were able to determine what types of identity-distinguishing information are encoded in different face-selective regions.

Materials and Methods

This study involved an fMRI component, in which we measured brain representations of faces and voices, and a behavioural component, in which we collected ratings of the same faces and voices on social traits and perceived similarity. The fMRI part corresponds to the same experiment and data described in Tsantani et al. (2019) and the behavioural part is reported here for the first time. In the present study, we analysed the data related to faces only.

Participants

We recruited thirty-one healthy right-handed adult participants to take part in two fMRI sessions and a behavioural session (all on separate days, resulting in at least six hours of testing per participant). We did not conduct a formal power analysis as there were no previous studies at the time of the study design that had investigated the main effect described in Tsantani et al. (2019). Our sample size was determined based on similar fMRI studies within the field and on available funding. To ensure adequate exposure to our stimulus set of famous people, participants were required to be native English speakers between 18 and 30 years of age, and to have been resident in the UK for at least 10 years. We also independently verified that all participants knew the famous people used in the experiment (please see Tsantani et al., 2019). No inclusion or exclusion criteria were applied based on race or ethnicity, and we did not formally record this information. It has been shown that the other-race effect does not apply to familiar faces (McKone et al., 2007; Zhou & Mondloch, 2016). Participants were recruited at Royal Holloway, University of London, and Brunel University London. One participant was excluded due to excessive head movement in the scanner. The final sample consisted of 30 participants (22 females, 8 males) with a mean age of 21.2 years ($SD=2.37$, range=19-27). Participants reported normal or corrected-to-normal vision and normal hearing, provided written informed consent, and were reimbursed for their participation. The study was approved by the Ethics Committee of Brunel University London.

Stimuli

The same stimuli were used in the fMRI and behavioural testing, and consisted of videos of the faces and sound recordings of 12 famous individuals, including actors, comedians, TV personalities, pop stars and politicians: Alan Carr, Daniel Radcliffe, Emma Watson, Arnold Schwarzenegger, Sharon Osbourne, Graham Norton, Beyonce Knowles, Barbara Windsor, Kylie Minogue, Barack Obama, Jonathan Ross, and Cheryl Cole. These individuals were selected based on pilot studies that showed that participants (aged between 18 and 30 and living in the UK) could recognise them easily from their faces and voices.

For each identity, six silent, non-speaking video clips of their moving face were obtained from videos on YouTube (Figure 1). The six clips were obtained from different original videos. In total, we obtained 72 face stimuli. Face videos were selected so that the background did not provide any cues to the identity of the person. The face videos were primarily front-facing and did not feature any speech but were otherwise unconstrained in terms of facial motion. Head movements included nodding, smiling, and rotating the head. Videos were edited so that they were three seconds long, 640 x 360 pixels, and centred on the bridge of the nose, using Final Cut Pro X (Apple, Inc.).

For purposes not related to this study, we also presented 72 voice stimuli, which consisted of recordings of the voices of the same 12 famous individuals (6 clips per identity) obtained from videos on YouTube. Speech clips were selected so that the speech content, which was different for every recording, did not reveal the identity of the speaker. Recordings were edited so that they contained three seconds of speech after removing long periods of silence using Audacity® 2.0.5 recording and editing software (RRID:SCR_007198). The recordings were converted to mono with a sampling rate of 44100, low-pass filtered at 10KHz, and root-mean-square (RMS) normalised using Praat (version 5.3.80; Boersma and Weenink 2014; www.praat.org).

Participants were familiarised with all stimuli via one exposure to each clip immediately before the first scanning session.

MRI data acquisition and preprocessing

Participants completed two MRI sessions: in each session, participants completed a structural scan, three runs of the main experiment, and functional localiser scans (for face and voice areas, but below we only describe the localiser of face-selective regions). Participants were scanned using a 3.0 Tesla Tim Trio MRI scanner (Siemens, Erlangen) with a 32-channel head coil. Scanning took place at the Combined Universities Brain Imaging Centre (CUBIC) at Royal Holloway, University of London. We acquired whole-brain T1-weighted anatomical scans using magnetization-prepared rapid acquisition gradient echo (MPRAGE) [1.0 x 1.0 in-plane resolution; slice thickness, 1.0mm; 176 axial interleaved slices; PAT, Factor 2; PAT mode, GRAPPA (GeneRalized Autocalibrating Partially Parallel Acquisitions); repetition time (TR), 1900ms; echo time (TE), 3.03ms; flip angle, 11°; matrix, 256x256; field of view (FOV), 256mm].

For the functional runs, we acquired T2*-weighted functional scans using echo-planar imaging (EPI) [3.0 x 3.0 in-plane resolution; slice thickness, 3.0mm; PAT, Factor 2; PAT mode, GRAPPA; 34 sequential (descending) slices; repetition time (TR), 2000ms; echo time (TE), 30ms; flip angle, 78°; matrix, 64x64; field of view (FOV), 192mm]. Slices were positioned at an oblique angle to cover the entire brain except for the most dorsal part of the parietal cortex. Each run of the main experiment comprised 293 brain volumes, and each run of the face localizer had 227 brain volumes.

Functional images were pre-processed using Statistical Parametric Mapping (SPM12; Wellcome Department of Imaging Science, London, UK; RRID:SCR_007037; <http://www.fil.ion.ucl.ac.uk/spm>) operating in Matlab (version R2013b; MathWorks; RRID:SCR_001622). The first three EPI images in each run served as dummy scans to allow for T1-equilibration effects and were discarded prior to pre-processing. Data from each of the two scanning sessions, which took place on different days, were first pre-processed independently with the following steps for each session. Images within each brain volume were slice-time corrected using the middle slice as a reference, and were then realigned to correct for head movements using the first image as a reference. The participants' structural image in native space was coregistered to the realigned mean functional image, and was segmented into grey matter, white matter, and cerebrospinal fluid. Functional images from the main experimental runs were not smoothed, whereas images from the localiser runs were smoothed with a 4-mm Gaussian kernel (full width at half maximum). To align the functional images from the two scanning sessions, the structural image from the first session was used as a template, and the structural image

from the second session was coregistered to this template; we then applied the resulting transformation to all the functional images from the second session.

Functional localisers and definition of regions of interest

Face-selective regions were defined using a dynamic face localiser that presented famous and non-famous faces, along with a control condition consisting of objects and scenes. The stimuli were silent, non-speaking videos of moving faces, and silent videos of objects and scenes, presented in an event-related design. Participants completed between one and two runs of the localiser across the two scanning sessions. The localiser presented different stimuli in each of two runs. For full details of the localiser please see Tsantani et al. (2019).

Functional regions of interest (ROIs) were defined using the Group-Constrained Subject-Specific method (Fedorenko et al., 2010; Julian et al., 2012), which has the advantage of being reproducible and reducing experimenter bias by providing an objective means of defining ROI boundaries. Briefly, subject-specific ROIs were defined by intersecting subject-specific localiser contrast images with group-level masks for each ROI obtained from an independent dataset. In this study, we obtained group masks of face-selective regions (right fusiform face area (rFFA), the right occipital face area (rOFA), and the right posterior superior temporal sulcus (rpSTS)) from a separate group of participants who completed the same localiser (for details see Tsantani et al., 2019). We focused on face-selective regions from the right hemisphere because they have been shown to be more consistent and larger compared to the left hemisphere (e.g. Rossion et al., 2012). Our masks are publicly available at <https://doi.org/10.17633/rd.brunel.6429200.v1>.

Contrast images were defined for each individual participant. Face-selectivity was defined by contrasting activation to faces versus non-face stimuli using *t*-tests. We then intersected these subject-specific contrasts with the group masks, and extracted all significantly activated voxels at $p < .001$ (uncorrected) that fell within the boundaries of each mask. In cases where the resulting ROI included fewer than 30 voxels, the threshold was lowered to $p < .01$ or $p < .05$. ROIs which included fewer than 30 voxels at the lowest threshold were not included, and this occurred for the rFFA in two participants and for the rOFA in one participant. For full details of size and location of all ROIs, please see Tsantani et al. (2019).

[Please insert Figure 1 about here]

Experimental Design and Statistical Analysis

Main experimental fMRI runs

In the main experimental runs, face stimuli were presented intermixed with voice stimuli within each run in an event-related design. The experiment was programmed using the Psychophysics Toolbox (version 3; RRID:SCR_002881; Brainard 1997; Pelli 1997) in Matlab and was displayed through a computer interface inside the scanner. Participants were instructed to fixate on a small square shape that was constantly present in the centre of the screen. From a distance of 85cm, visual stimuli subtended 20.83 x 12.27 degrees of visual angle on the 1024 x 768 pixel screen.

The experiment was presented in two scanning sessions, with three runs in each session. Each run featured two unique videos of the face of each of the 12 identities,

presented twice. Each run therefore contained 48 face trials (12 identities x 2 videos x 2 presentations), intermixed with 48 voice trials (96 experimental trials in total). In other words, across all three runs within a session, each of the 12 face identities appeared in 12 trials, featuring six unique videos of their face. Stimuli were presented in a pseudorandom order that prohibited the succeeding repetition of the same stimulus and ensured that each identity could not be preceded or succeeded by another identity more than once within the same modality. Each trial presented a stimulus for 3000 ms and was followed by a 1000 ms ITI (Figure 1).

To maintain attention to stimulus identity in the scanner, participants performed an anomaly detection task in which they indicated via button press when they were presented with a famous face or voice that did not belong to one of the 12 famous individuals that they had been familiarised with prior to the experiment. Therefore, each run also included 12 randomly presented task trials (six faces & six voices). Finally, each run contained 36 randomly interspersed null fixation trials, resulting in a total of 144 trials in each run lasting around 10 minutes.

The three experimental runs that were completed in the first scanning session were repeated in the second session with the same stimuli, but in a new pseudorandom order. The task stimuli, however, were always novel for each run. The three runs, which had different face videos, were presented in counterbalanced order across participants in both sessions.

Behavioural session

All participants completed a behavioural session in a laboratory, which took place on a separate day and always after the fMRI sessions had been completed. In this session, participants rated the same faces that they had been presented with in the scanner on perceived social traits and on perceived pairwise visual similarity. Participants also rated voices (the order of tasks was counterbalanced across modality), but these results are not presented here. All tasks and stimuli were presented using the Psychophysics Toolbox and Matlab.

Social Trait Judgement Tasks

In the social trait judgement tasks, participants were asked to make judgements about the perceived trustworthiness, dominance, attractiveness, and positive-negative valence of the face identities. There were four blocks, one for each judgement, and their order was counterbalanced across participants. Face stimuli were presented in the centre of the screen. In contrast to the fMRI runs, in which stimuli were presented for the full three seconds of their duration, here all stimuli were only presented for the first 1500 ms of their duration, to reduce testing time.

All blocks followed the same trial structure (Figure 1). In each trial, a face identity was presented with three videos — these were presented successively with no gap in between them (total of 4500 ms). Participants were then asked to rate how trustworthy/dominant/attractive/negative-positive the face was, and they were asked to base their judgement on all three videos of the face. The rating scale ranged from 1 (very untrustworthy/non-dominant/unattractive/negative) to 7 (very trustworthy/dominant/attractive/positive) and participants responded using the corresponding keys on the keyboard. There was a 1000ms ITI following the response.

Each identity was presented in two trials; one trial presented three face videos randomly selected from the six available, and the other trial presented the remaining three videos. This resulted in 24 trials in each block (12 identities x 2 presentations). The videos within each trial were presented in a random order, and the trial order was also randomised. Trustworthiness was defined as 'able to be relied on as honest and truthful'. Dominance was defined as 'having power and influence over other people'. No definition was deemed necessary for valence or attractiveness. Participants were advised that there was no time limit to their responses and that they should follow their first judgment. The duration of each block was approximately 3 minutes.

Pairwise Visual Similarity Task

In the pairwise similarity task, participants rated the perceived visual similarity of pairs of face identities. Each of the 12 identities was paired with the other 11 identities creating 66 identity pairs. Each identity was presented by three videos, randomly selected from the six available videos. Each identity pair was presented in two trials, counterbalancing the presentation order of each identity in the pair. There were therefore 132 trials in each task (66 identity pairs x 2 presentations). The presentation order of the pairwise similarity tasks in relation to the social trait judgement tasks was also counterbalanced across participants.

Participants were instructed to rate the similarity between the visual appearance of the two face identities in each pair, focusing on the facial features. Participants were asked to rate how similar the two faces looked on a scale from 1 (very dissimilar) to 7 (very similar). Participants were advised that there was no time limit to their responses and that they should follow their first instinct. Participants were told to ignore similarities between people that were related to biographical or semantic information (e.g. if both identities were actors). Furthermore, to encourage participants to base their judgements on perceptual information, participants were advised to consider to what extent two identities could potentially be related to each other, i.e. be part of the same family, based on how they looked.

In each trial, participants were first presented with the three videos of the face of one identity (Figure 1). Following a 500ms fixation screen, they were presented with the three videos of the face of the second identity. Videos for each identity were presented successively with no gap in between. Each video was presented for 1500ms and there was a 1000ms ITI following the response. The presentation order of the trials was randomised. The duration of each task was approximately 30 minutes.

Brain Representational dissimilarity matrices (RDMs)

Representational dissimilarity matrices (RDMs) showing the discriminability of the brain response patterns elicited by the 12 face identities (during the fMRI experimental runs) were created for each individual participant and for each ROI.

First, to obtain brain responses at each voxel for each of the 12 face identities, mass univariate time-series models were computed for each participant using a high-pass filter cutoff of 128 seconds and autoregressive AR(1) modelling to account for serial correlation. Regressors modelled the BOLD response at stimulus onset and were convolved with a canonical hemodynamic response function (HRF). We defined a model for each run separately, and for every possible pair of runs within a scanning session (by concatenating the two runs), to create data partitions for cross-validation (described below). Each model contained a regressor for the face of each of the 12 identities, which incorporated the

different videos of their face (two per run) and the repetitions of those videos. The model also included regressors for each of the 12 voice identities, task trials, and the six motion parameters obtained during the image realignment preprocessing stage (included as regressors of no interest).

Second, within each ROI, we extracted the beta estimates at each voxel for each of the 12 face identities. This resulted in 12 vectors of beta values per ROI that described the response patterns (across voxels) elicited by the 12 face identities.

Third, these vectors of beta estimates were used to compute 12x12 Face RDMs in face-selective ROIs, in which each cell showed the distance between the response patterns of two identities (Figure 2B). RDMs were computed using the linear discriminant contrast (LDC), a cross-validated distance measure (Nili et al. 2014; Walther et al. 2016), which we implemented using in-house Matlab code and the RSA toolbox (Nili et al. 2014). Two RDMs were created for each ROI, one for each scanning session. Each RDM was computed using leave-one-run-out cross-validation across the three runs, which presented different stimuli for each identity. Therefore, RDMs showed the dissimilarities between face *identities*, rather than specific face videos. In each cross-validation fold, concatenated data from two runs formed partition A, and data from the left-out run formed partition B. For each pair of identities (e.g. ID1 and ID2), partition A was used to obtain a linear discriminant, which was then applied to partition B to test the degree to which ID1 and ID2 could be discriminated. Under the null hypothesis, LDC values are distributed around zero when two patterns cannot be discriminated. Values higher than zero indicate higher discriminability of the two response patterns (Walther et al. 2016).

The discriminability of face identities in each ROI was computed by calculating the mean LDC across all cells of each participant's RDM, and comparing the mean LDC distances against zero (Tsantani et al., 2019).

Full details of this analysis are presented in Tsantani et al (2019) and the data to compute brain RDMs are available at <https://doi.org/10.17633/rd.brunel.6429200.v1>. Here, we used the RDMs for three face-selective regions (rFFA, rOFA, and rpSTS). All three of these regions showed significant discriminability of face identities.

RDMs based on image-computable properties

We computed dissimilarities between the 12 face identities based on visual descriptions of their faces obtained using the models described below. We did not use the full videos as input to these models, but instead extracted one still frame from each face video used in the experiment (typically the first frame in which the full face was visible and the image was not blurred). Thus, we obtained six different images of the face of each identity, taken from the six different videos in which the identity was presented, resulting in 72 images in total.

OpenFace Model

The 'OpenFace' model RDM was computed from low-dimensional face representations obtained from OpenFace (Amos et al., 2016; <http://cmusatyalab.github.io/openface/>). Briefly, OpenFace uses a deep neural network that has been pre-trained (using 500,000 faces) to learn the best features or measurements that can group two pictures of the same identity together and distinguish them from a picture of a different identity. We used this pre-trained neural network to generate measurements for each of our face pictures and to compare these measurements between each pair of pictures. OpenFace first performs

face-detection, identifies pre-specified landmarks, and does an affine transformation so that the eyes, nose and mouth appear in approximately the same location. The faces are then passed on to the pre-trained neural network to generate 128 descriptor measurements for each face. To create an RDM, we used the program's calculated distances between the measurements for each pair of faces images. A value of zero indicates that two images are identical, and values between 0 and 1 suggest that two different images likely show the same person's face. Values higher than 1 indicate that the two images show the faces of two different people. We found that OpenFace performed well at grouping different images of the same person's face compared to images of different people's faces in our image set — Extended Data Figure 2-1 includes full 72x72 matrices showing distances between all images, *but these full matrices were not used in any analysis*). To obtain a 12x12 RDM for the 12 identities, which would be comparable to the brain RDMs, we computed the mean of all cells that showed images of the same identity pair (Figure 2C). *The 12x12 RDMs were used in all analyses.*

Gabor-Jet Model

The Gabor-Jet model RDM was computed from visual descriptors of face images obtained using the Gabor-Jet model (Biederman & Kalocsai, 1997; Margalit et al., 2016; Yue et al., 2012). This model was designed to simulate response properties of cells in area V1, and has been found to correlate with psychophysical measures of facial similarity (Yue et al., 2012). In addition, Carlin and Kriegeskorte (2017) showed that the dissimilarity of response patterns to different faces in the FFA was predicted by image properties based on Gabor filters. First, we used OpenFace 2.0 (Baltrusaitis et al., 2018) to automatically detect the faces in each image, and the pictures were greyscaled. The Matlab script provided in www.geon.usc.edu/GWTgrid_simple.m was then used to create a 100 x 40 Gabor descriptor for each face. After transforming these matrices into vectors, we computed the Euclidean distance between the vectors from each pair of faces (Extended Data Figure 2-1), and then averaged the distances across all pairs of stimuli that showed the same two identities, *resulting in a 12x12 RDM* (Figure 2C).

GIST Model (Faces only and whole Frames)

The Gist model RDMs were computed from visual descriptors of pictures obtained using the GIST model (Oliva and Torralba, 2001). The GIST model estimates information about the spatial envelope of scenes and it is related to perceived dimensions of naturalness, openness, roughness, expansion, and ruggedness. Weibert et al. (2018) showed that the similarity between the representations of different faces in the FFA, OFA, and posterior STS was predicted by the similarity of the different pictures computed using the GIST descriptor model. We extracted GIST descriptors both from the full picture (whole Frames) and just from the face (Faces only - we used the same stimuli as in the Gabor-Jet model). We then used the Matlab script provided in <http://people.csail.mit.edu/torralba/code/spatialenvelope> to compute GIST descriptors for each picture, and computed Euclidean distances between each pair of pictures (Extended Data Figure 2-1). We finally averaged the distances across all pairs of stimuli that showed the same two identities, *resulting in 12x12 RDMs* (Figure 2C).

Pixel Model (Faces only and whole Frames)

Finally, we computed model RDMs based on pixel dissimilarity between each pair of pictures. Like for the GIST model, we computed this model both for the full picture (whole Frames) and just for the face (Faces only). We extracted pixel greyscale values for each image, computed Pearson correlations between the vectors of each pair of images, and

used correlation distance as the output measure ($1 - r$) (Extended Data Figure 2-1). We finally averaged the distances across all pairs of stimuli that showed the same two identities, resulting in 12x12 RDMs (Figure 2C).

RDMs based on Perceived properties

Social Trait Models: Trustworthiness, Dominance, Attractiveness, Valence, Social Traits (All)

RDMs for ratings of the 12 face identities on trustworthiness, dominance, attractiveness, and positive-negative valence were computed using Euclidean distances. For each participant and each social trait, the Euclidean distance between the ratings of each pair of identities was calculated (ratings were averaged across the two trials in which the same identity was presented), resulting in a 12x12 RDM per trait. We then averaged the matrices for the same trait across participants (Figure 2C).

We also created 'Social Traits (All)' RDMs combining all four social traits, by calculating the Euclidean distance between all trait ratings for each pair of identities, resulting in a 12x12 trait RDM per participant. We then computed the mean matrix for all social traits across participants (Figure 2C).

To get estimates of the inter-subject reliability of these models, we computed the correlations between each participant's RDM and the average RDMs across all participants (i.e. the RDMs that we used as models), and then averaged the correlations across participants. The reliabilities were $r = .34$ for Trustworthiness, $r = .48$ for Dominance, $r = .67$ for Attractiveness, $r = .31$ for Valence, and $r = .48$ for Social Traits (All). We also computed the average correlations between each participant's RDM and the average RDM of all remaining participants. These reliabilities were $r = .24$ for Trustworthiness, $r = .42$ for Dominance, $r = .63$ for Attractiveness, $r = .20$ for Valence, and $r = .42$ for Social Traits (All).

Perceived Similarity Model

The judgements in the Pairwise Visual Similarity Task indicated the degree of visual similarity between all possible pairs of identities. These ratings were averaged across the two trials in which each identity-pair was presented, and were reverse-coded to match the LDC and Euclidean distance measures, where a higher value indicates higher dissimilarity. The resulting values were arranged into a 12x12 face RDM for each participant and were then averaged across participants (Figure 2C).

Inter-subject reliability, estimated by computing the average correlation between each participant's RDM and the average RDMs across all participants, was $r = .65$. Reliability computed as the average correlation between each participant's RDM and the average RDM of all remaining participants was $r = .61$.

Gender Model

Finally, a 12x12 RDM for gender was constructed by assigning a value of 0 to same gender identity pairs, and a value of 1 to different-gender identity pairs (Figure 2C).

Correlations between all 13 models are presented in Figure 2D and Extended Data Figure 2-2.

[Please insert Figure 2 about here]

Individual model analysis: RSA comparing brain RDMs to candidate model RDMs using correlation

For each individual participant and each ROI, we compared the brain RDM for faces with each of the candidate model RDMs defined above using Pearson correlation (Figure 3A). We then tested whether the correlations across participants for each ROI were significantly higher than zero, using two-sided one-sample Wilcoxon signed-rank tests (Nili et al., 2014). P-values were corrected for multiple comparisons using FDR correction ($q=.05$) across all 13 comparisons for each ROI. We also compared the correlations across all pairs of models within each ROI, in order to test which model was the best predictor of the variance in brain RDMs in each ROI. For these pairwise comparisons, we used two-sided Wilcoxon signed-rank tests and only significant FDR corrected values (for 78 comparisons) are reported.

An estimate of the noise ceiling was calculated for each ROI, in order to estimate the maximum correlation that any model could have with the brain RDMs in each ROI given the existing noise in the data. We estimated the noise ceiling using the procedures described by Nili et al. (2014). The lower bound of the noise ceiling was estimated by calculating the Pearson correlation of the brain RDM for each participant with the average brain RDM across all other participants (after z-scoring the brain RDM for each participant). The upper bound of the noise ceiling was estimated by computing the Pearson correlation of the brain RDM for each participant with the average brain RDM across all participants (after z-scoring the brain RDM for each participant).

Weighted model-combination analysis: Weighted representational modelling

We also used weighted representational modelling (Khaligh-Razavi & Kriegeskorte, 2014; Jozwik et al., 2016; 2017) to combine individual models via reweighting and thus investigate if combinations of different model RDMs could explain more variance in representational geometries than any single model. For each combined model, we used linear non-negative least squares regression (lsqnonneg algorithm in Matlab) to estimate a weight for each component of the combined model. We fitted the weights and tested the performance of the reweighted (combined) model on non-overlapping groups of both participants and stimulus conditions within a cross-validation procedure, and used bootstrapping to estimate the distribution of the combined model's performance (Storrs et al., 2020).

We used six different combinations of component models: *Image-computable* properties (OpenFace, GIST, GaborJet, and Pixel), *Social Traits* (comprising a weighted combination of the Trustworthiness, Dominance, Attractiveness, and Valence properties), *Perceived* properties (Trustworthiness, Dominance, Attractiveness, Valence, Perceived Similarity, and Gender), *Low-Level* properties (GIST, GaborJet, and Pixel), *High-Level* properties (Trustworthiness, Dominance, Attractiveness, Valence, Perceived Similarity, Gender, and OpenFace), and *All properties*.

Within each crossvalidation fold, data from eight participants for four stimulus identity conditions was assigned to serve as test data, and the remainder was used to fit the weights for each component of each of the six combined models. Because the crossvalidation was performed within a participant-resampling bootstrap procedure, the number of participant data RDMs present in each crossvalidation fold was sometimes smaller than eight (when a participant was not present in the bootstrap) or larger than eight (when a participant was sampled multiple times in the bootstrap). All data from the same participant was always assigned *only* to either the training or test split. A reweighting

target RDM was constructed by averaging the training-split participants' RDMs for training-split stimulus conditions, and weights were fitted to the components of each combined model to best predict this target RDM. The six resulting combined models, as well as the 13 individual models, were then correlated separately with each of the brain RDMs from test participants for test conditions, using Pearson correlation. The noise ceiling was also computed within every cross-validation fold using the same procedure as for the main analysis. In other words, we correlated (Pearson correlation) each test participant's RDM with the average of all other test RDMs excluding their own (for the lower bound of the noise ceiling) and with the average of all test participants' RDMs including their own (for the upper bound of the noise ceiling). This procedure was repeated for 30 participant crossvalidation folds within 30 stimulus-condition crossvalidation folds to provide a stabilised estimate of the noise ceiling and the performance of each model (Storrs, et al., 2020).

The cross-validation procedure was repeated for 1,000 bootstrap resamplings of participants for each face-selective ROI. From the resulting bootstrap distribution, we computed the mean estimate of the lower bound of the noise ceiling, as well as the mean of each model's correlation with human data for both individual models and combined models (Figure 3B). Correlations between model and brain RDMs were considered significantly higher than zero if the 95% confidence interval of the bootstrap distribution did not include zero. Bonferroni correction was applied to correct for multiple comparisons. Finally, we compared each pair of models by testing whether the distributions of the differences between each pair of models contained zero. We only report pairwise differences that were significant after Bonferroni correction. Code for this analysis was adapted from here: https://github.com/tinyrobots/reweighted_model_comparison.

Data and code accessibility

Data and code for main analysis are available here:
<https://doi.org/10.25383/city.11890509.v1>

Results

We tested 30 participants in an fMRI experiment, in which they were presented with faces of 12 famous people (same fMRI data as in Tsantani et al., 2019), and in a separate behavioural experiment, in which participants rated the faces of the same people on perceived similarity and social traits (Figure 1). We then computed representational dissimilarity matrices (RDMs) showing the representational distances between the brain response patterns elicited by the face identities in the face-selective right FFA, OFA, and pSTS. The distance measure that we used to compute the RDMs was the linear discriminant contrast (LDC), which is a crossvalidated estimate of the Mahalanobis distance (Walther et al., 2016). The mean LDC across each RDM showed that response patterns to different face identities were discriminable in all three regions (Tsantani et al., 2019). To investigate the informational content of brain representations of the face identities in each face-selective region, we used RSA (Kriegeskorte et al., 2008a; 2008b) to compare the brain RDMs with a diverse set of candidate model RDMs (Figure 2). We used candidate models based on the physical properties of the stimuli (*image-computable models*), including low-level stimulus properties (based on Pixel-wise, GIST (Oliva & Torralba, 2001) and Gabor-jet (Biederman & Kalocsai, 1997) dissimilarities) and higher-

level image-computable descriptions obtained from a deep neural network trained to cluster faces according to identity (OpenFace; Amos et al., 2016) (see Methods). Additionally, we used candidate models based on perceived higher-level properties (*perceived-property models*), including Gender and participants' ratings of the face identities on Perceived Similarity and Social traits (Trustworthiness, Dominance, Attractiveness, Valence, and Social Traits (All) — which corresponds to all traits combined) in a behavioural experiment.

[Please insert Figure 3 about here]

Individual model analysis

In our main analysis, we computed Pearson's correlations between RDMs in the right FFA, OFA, and pSTS, and each candidate model RDM. Correlations were computed for each individual participant, and then correlations across participants for each model were compared against zero using two-sided one-sample Wilcoxon signed-rank tests. For each ROI and each model that showed significant correlations with participants' brain RDMs, we report below the mean correlation across participants, and the Z statistic and p-value obtained from the signed-rank test, corrected for multiple comparisons using FDR correction. Full results are presented in Figure 3A and Table 1, and individual-subject correlations are presented in Figure 4. We also compared the correlations across all pairs of models using two-sided Wilcoxon signed-rank tests.

Brain RDMs in the right FFA had the highest mean correlation with the Perceived Similarity model (mean $r = .11$, $Z = 3.69$, $p = .0002$), followed by perceived Social Traits (All) (mean $r = .10$, $Z = 2.71$, $p = .0067$), the image-computable neural network OpenFace (mean $r = .10$, $Z = 3.46$, $p = .0005$), perceived Attractiveness (mean $r = .09$, $Z = 2.69$, $p = .0072$), Gender (mean $r = .09$, $Z = 3.30$, $p = .0010$), and Valence (mean $r = .06$, $Z = 2.39$, $p = .0168$) (Figure 3A). We estimated the lower bound of the noise ceiling as the mean correlation between each participant's FFA RDM and the average of all other participants' FFA RDMs (Nili et al., 2014). This estimates the non-noise variance in the data, and is not overfit to the present data. None of the mean correlations reached the lower bound of the noise ceiling for the FFA ($r = .14$) — this suggests that there could be models outside those tested here that would better explain the representational distances in FFA. Pairwise comparisons showed no significant differences between the correlations of any pairs of models (all $p > .0041$; no significant results after FDR correction).

In contrast with the FFA, the brain RDMs in the right OFA had the highest mean correlations with low-level image-computable models. The highest mean correlation was observed with the Pixel-Faces model (mean $r = .22$, $Z = 4.36$, $p < .0001$) (Figure 3A), followed by the Gabor-Jet (mean $r = .20$, $Z = 3.97$, $p < .0001$), Pixel-Frames (mean $r = .11$, $Z = 3.02$, $p = .0026$), GIST-Faces (mean $r = .10$, $Z = 2.22$, $p = .0267$), perceived Attractiveness (mean $r = .09$, $Z = 2.84$, $p = .0045$), Gender (mean $r = .07$, $Z = 2.76$, $p = .0058$), and the OpenFace model (mean $r = .07$, $Z = 2.95$, $p = .0032$). None of the mean correlations reached the lower bound of the noise ceiling ($r = .34$). Pairwise comparisons between model correlations revealed that the Pixel-Faces model had significantly higher correlations with the OFA RDMs than all other models (all $p < .0058$, FDR corrected), except for the Gabor-Jet model and the GIST-Faces model. The Gabor-Jet model also had significantly higher correlations with the brain RDMs in OFA than all other models (all $p < .0058$, FDR corrected), except the Pixel-Faces and Pixel-Frames models. Perceived Attractiveness had significantly higher correlations with the OFA RDMs than perceived

Valence ($p = .0051$), and Social traits (All) was significantly higher than Trustworthiness and Valence (both $p < .0018$).

Finally, we investigated which model best explained the variance in representational distances in the right pSTS. We found no significant correlations between any of the candidate models and the brain RDMs in this region (all $p > .0333$; no significant results after FDR correction) (Figure 3A). None of the models reached the lower bound of the noise ceiling ($r = .13$), and there were no significant differences between models (all $p > .0140$; no significant results after FDR correction).

[Please insert Table 1 about here]

[Please insert Figure 4 about here]

These results show a clear distinction between the types of models that were associated with the representational geometries of face-identities in the FFA and OFA. Representational distances of face identities in the FFA were most associated with high-level perceived similarity, gender, and social traits, as well as a high-level model of image-computable properties (OpenFace), whereas representations in OFA were most associated with low-level image-computable properties. To test this directly, we compared the correlation profiles between the two regions. We first averaged all correlations per participant (after Fisher's transformation) for the same type of model (all perceived-property models and all image-computable models) for each ROI (FFA and OFA). In the FFA, the mean correlation with perceived-property models was .08 ($SD = .095$) and .03 ($SD = .109$) with image-computable models. In the OFA, the mean correlation with perceived-property models was .05 ($SD = .108$) and .13 ($SD = .102$) with image-computable models. We then conducted a 2-by-2 repeated measures ANOVA with ROI and type of model as variables. There was no main effect of ROI ($F(1,27)=3.37$, $p=.0773$) or type of model ($F(1,27)=.36$, $p=.5519$), but there was a significant interaction between the two variables ($F(1,27)=23.75$, $p<.0001$). Pairwise comparisons (using two-sided Wilcoxon signed-rank tests) showed that in the FFA, the correlations with perceived-property models were significantly higher than correlations with image-computable models ($Z = 2.25$, $p = .0242$), whereas in the OFA, correlations with perceived-property models were significantly lower than correlations with image-computable models ($Z = -3.17$, $p = .0015$). We also divided the models into low-level properties (GIST, Gabor-Jet, and Pixel) and high-level properties (Trustworthiness, Dominance, Attractiveness, Valence, Perceived Similarity, Gender, and OpenFace), and computed means per participant and per ROI for each of these types of models. In the FFA, there was a mean correlation of .08 ($SD = .090$) with high-level properties, and of .02 ($SD = .157$) with low-level properties. In the OFA, there was a mean correlation of .05 ($SD = .102$) with high-level properties, and of .16 ($SD = .141$) with low-level properties. A 2-by-2 repeated measures ANOVA showed a significant effect of ROI ($F(1,27)=5.44$, $p=.0274$), no significant effect of model ($F(1,27)=.43$, $p=.5201$), and a significant interaction between the two variables ($F(1,27)=21.64$, $p<.0001$). Pairwise comparisons showed that in the FFA, the correlations with high-level models were significantly higher than correlations with low-level models ($Z = 2.21$, $p = .0272$), whereas in the OFA, correlations with high-level models were significantly lower than correlations with low-level models ($Z = -3.25$, $p = .0011$). These results demonstrate the clear distinct patterns of correlations for the FFA and OFA.

[Please insert Figure 5 about here]

Our image-computable models used a single image from each video clip. We re-computed all models using 72 images per clip, and averaged the features across all images of the same clip. We then computed distances between video clips in the same manner as before, and averaged distances for each pair of identities, resulting in 12x12 RDMs for each model. The results were very similar when using 72 images per clip compared to one image per clip (Figure 5A). We additionally showed that we obtained similar results to those in Figure 3A when using other similarity measures between RDMs (Spearman correlation, Kendall tau-a), demonstrating that these results are not dependent on using Pearson correlation (Figure 6). Finally, we conducted an additional control analysis using brain RDMs in the same ROIs but built from response patterns to voices of the same individuals, instead of brain responses to faces. There were no significant correlations between any of the model RDMs for faces and brain RDMs for voices after correcting for multiple comparisons in the rFFA (all $p > .040$), rOFA (all $p > .103$), or rpSTS (all $p > .063$) (Figure 7). Pairwise comparisons showed no significant differences between the correlations of any pairs of models (all $p > .034$). The estimated lower bounds of noise ceilings for the voices brain RDMs were very low for rFFA ($r = -.038$) and rOFA ($r = -.001$), and higher for rpSTS ($r = .108$). This control analysis demonstrates that the above results for FFA and OFA are specific to visual stimuli (faces). To conclude, we find that the structure of the model correlations is reliable and is systematically different between the FFA and OFA.

[Please insert Figure 6 about here]

[Please insert Figure 7 about here]

Weighted model-combination analysis

Although our models accounted for a large portion of the explainable variance (based on the noise ceiling) in brain representations in the right FFA and OFA, none of the mean correlations reached the lower bound of the noise ceiling. It could be that each individual model captured only a portion of the information represented in each brain region, in which case we may be able to fully explain the brain representations by combining multiple models. We thus used weighted representational modelling (Khaligh-Razavi & Kriegeskorte, 2014; Jozwik et al., 2016; Jozwik et al., 2017) to combine sets of models into weighted combinations via crossvalidated fitting on the human data, and to investigate if these combined models resulted in better predictions of the brain dissimilarities in each brain region (see Methods). We considered six different combined models: *Image-computable* properties (OpenFace, GIST, GaborJet, and Pixel), *Social Traits* (comprising a weighted combination of the Trustworthiness, Dominance, Attractiveness, and Valence properties), *Perceived* properties (Trustworthiness, Dominance, Attractiveness, Valence, Perceived Similarity, and Gender), *Low-Level* properties (GIST, GaborJet, and Pixel), *High-Level* properties (Trustworthiness, Dominance, Attractiveness, Valence, Perceived Similarity, Gender, and OpenFace), and *All properties*.

We used linear non-negative least squares regression to estimate a weight for each component of each combined model. We fitted the weights and tested the performance of the reweighted (combined) model on non-overlapping groups of both participants and stimulus conditions within a cross-validation procedure, and used bootstrapping to estimate the distribution of the combined model's performance (Storrs et al., 2020). Figure 3B shows the results of this analysis. P-values were corrected for multiple comparisons using Bonferroni correction. For the FFA, the combined models for Perceived properties and High-Level properties had the highest mean correlations with the brain RDMs, and the

individual-subject correlations were significantly above zero. For the OFA, the combined model of all Low-Level properties and that of all image-computable properties had the highest mean correlations with the brain RDMs, although the individual-subject correlations were not significantly above zero after correcting for multiple comparisons. Importantly, however, none of the combined models performed better than the best of the individual models (see full results in Table 2). Instead, the models with best performance in the previous (main) analysis also showed the highest correlations in this analysis. These results suggest that the models that best explained representational distances in each face-selective region share overlapping variance, given that combining them did not improve model performance. Lastly, replicating the findings of the previous analysis using more stringent statistical methods (crossvalidation across stimuli and participants) provides further evidence of a reliable pattern of model correlations in FFA and OFA that reveals a distinction between the type of information encoded in these two regions.

[Please insert Table 2 about here]

Individual differences and idiosyncratic representations

It is possible that there were substantial individual differences in face identity representations that limit the magnitude of the correlations between brain and model RDMs in our analyses. Brain and behavioural representations of face identities could be idiosyncratic and thus characteristic of each individual. We considered below three ways in which we could test this hypothesis.

First, we considered whether there were substantial individual differences in brain RDMs. To estimate the lower-bound of the noise ceiling, we had computed inter-subject reliabilities of brain RDMs. If, however, there were substantial individual differences in the brain RDMs, we would expect that representational distances in each of the face-selective ROIs could be highly reliable within each participant but not across participants. We thus computed intra-subject reliabilities of brain RDMs by correlating the brain RDMs calculated independently from two separate testing sessions for each participant, and then averaging the correlations across participants. We note that in all other analyses in the present manuscript, the brain RDMs for each participant corresponded to the average of these two sessions. For all three face-selective ROIs, we observed intra-subject reliabilities ($r_{\text{FFA}} = .063$; $r_{\text{OFA}} = .079$; $r_{\text{pSTS}} = .094$) that were on average lower than the inter-subject reliabilities ($r_{\text{FFA}} = .135$; $r_{\text{OFA}} = .337$; $r_{\text{pSTS}} = .126$ — please see Table 1), suggesting that in fact, in this case, the brain RDMs were not more reliable within each individual. It is important to note, however, that there was much less data to compute intra-subject reliabilities than inter-subject reliabilities.

Second, idiosyncratic brain representations could also result in higher correlations between each participant's brain RDM and behavioural RDMs based on their own ratings, compared to the average behavioural RDMs that we used in the main analyses. We thus repeated the main analysis using each individual's own RDMs for the rating-based perceived-property models, namely Perceived Similarity, Trustworthiness, Dominance, Attractiveness, Valence, and Social Traits (All). The results, however, did not reveal higher correlations when using these participant-specific behavioural models (Figure 5B). In contrast, correlations with the participants' individual behavioural models were slightly lower than when using average behavioural models.

A third possibility is that idiosyncratic representational geometries could result in the variance of each participant's brain RDMs being best explained by a uniquely weighted

combination of candidate models (even if no set of weightings would perform well for all participants). However, we did not have sufficient data per participant to test this possibility here.

Discussion

We aimed to investigate what information is explicitly encoded in the face-selective right FFA, OFA, and pSTS. We extracted fMRI patterns elicited by famous face identities in these regions, and computed face identity RDMs which showed that face identities could be distinguished based on their elicited response patterns in all three regions. Using RSA, we compared the brain RDMs for the FFA, OFA, and pSTS with multiple model RDMs ranging from low-level image-computable properties (pixel-wise, GIST, and Gabor-jet dissimilarities), through higher-level image-computable descriptions (OpenFace deep neural network, trained to cluster faces by identity), to complex human-rated face properties (perceived visual similarity, social traits, and gender). We found that the FFA and rOFA encode face identities in a different manner, suggesting distinct representations in these two regions. The representational geometries of face identities in the FFA were most associated with high-level properties, such as perceived visual similarity, social traits, gender, and high-level image features extracted with a deep neural network (OpenFace; Amos et al., 2016). In contrast, the representational geometries of faces in the right OFA were most associated with low-level image-based properties, such as pixel similarity and features extracted with Gabor filters that simulate functioning of early visual cortex. While previous studies had shown that low-level properties of images extracted with Gabor filters were associated with representational distances of faces in right FFA (Carlin & Kriegeskorte, 2017; Weibert et al, 2018), our results suggest that representations in right FFA use more complex combinations of stimulus-based features and relate to higher-level perceived and social properties (see also Davidesco et al., 2014). These results inform existing neurocognitive models of face processing (Haxby et al., 2000; Duchaine & Yovel, 2015) by shedding light on the much-debated computations of face-responsive regions, and providing new evidence to support a hierarchical organisation of these regions from the processing of low-level image-computable properties in the OFA to higher-level visual features and social information in the FFA.

Our initial prediction was that by combining and reweighting different candidate models, we would be better able to explain the brain RDMs. However, we did not find evidence for this in any of our face-selective ROIs. These results suggest that, when more than one model was significantly correlated with the brain RDMs for a certain brain region, they tended to explain overlapping variance in the brain RDMs. For example, while Perceived Similarity and OpenFace both explained the representational geometries in right FFA, their combination did not explain more variance than each model individually. However, our pattern of results suggests a clear distinction between the *types* of models that are associated with representations in the FFA and OFA, with higher-level properties explaining more variance in the FFA, and lower-level image-based properties explaining more variance in the OFA.

One crucial aspect of our study is that we used naturalistically varying video stimuli and multiple depictions for each identity. Brain RDMs were built by cross-validating the response patterns across runs featuring different videos of the face of each identity, and behavioural models were based on averages of ratings of multiple videos for each identity. Image-based models were built by calculating dissimilarities between image frames taken

from multiple videos of the face of each identity, and then computing the mean dissimilarity across different image pairs featuring the same identity pair. Behavioral studies have demonstrated that participants make more mistakes in “telling together” (i.e. grouping multiple images of the same identity, which is different process from “telling apart”, or distinguishing, between different identities) different photos of the same person when those photos were taken with different cameras, on different days, or with different lighting conditions, compared to when photos were taken on the same day and with the same camera (Bruce et al, 1999, Jenkins et al, 2011). Most previous fMRI studies, however, used very visually similar images, or even just a single image, for each identity, making it difficult to determine whether a brain region represents different *face images* or different *face identities*. Here, by having multiple videos for each person we can be more confident that we are capturing representations of specific identities rather than specific stimuli.

Related to the previous point, Abudarham and Yovel (2016) have recently shown that humans are more sensitive in perceiving changes in some face features (such as lip-thickness, hair, eye colour, eye shape, and eyebrow thickness) compared to others (such as mouth size, eye distance, face proportion, skin color). Changes in the former type of features (a.k.a. critical features) are perceived as changes in identity and those features tend to be invariant for different images of the same identity. Interestingly, Abudarham et al (2019) showed that the OpenFace algorithm that we used in the present study also seemed to be capturing those same critical features. Given our results in right FFA, it would be interesting to see whether representations in this region can also distinguish between the processing of the critical and non-critical face features as described by Abudarham and colleagues (2016; 2019).

Grossman and colleagues (2019) have also recently shown that representations in the FFA relate to image-computable descriptors from a deep neural network. There are two main differences, however, between our results and those of Grossman et al (2019). First, Grossman et al (2019) found similar representational geometries across all face-selective ventral temporal cortex, and no differentiation between OFA and FFA. One possible reason for this difference is that the authors were only able to define OFA and FFA in the left hemisphere, whereas our face-selective regions were defined in the right hemisphere. Face-selective regions are more consistent and larger in the right hemisphere (e.g. Rossion et al, 2012). A second main difference between our results and those of Grossman et al (2019) is that the deep neural network that we used here showed high generalisation across different images of the same person. OpenFace (Amos et al., 2016) was trained specifically to group together images of the same person and distinguish images of different people, and it performed very well in doing this in our set of stimuli (see Extended Data Figure 2-1), where it showed high generalisation across very variable pictures of the same person. This was not the case with the VGG-Face network used by Grossman et al (2019). Future studies should focus on describing and comparing the image-level descriptions of different types of neural networks.

Previous studies have demonstrated that face-selective regions are sensitive to the viewpoint from which faces are presented (Grill-Spector et al., 1999; Axelrod and Yovel, 2012; Kietzmann et al., 2012; Ramírez et al., 2014; Dubois et al., 2015; Guntupalli et al., 2017). However, there is also evidence that the FFA, OFA, anterior temporal lobe, and pSTS represent face identity across different viewpoints (Anzellotti et al., 2014; Anzellotti and Caramazza, 2017; Guntupalli et al., 2017). In our video stimuli, the faces were mostly

front-facing, but were free to vary in terms of changes in viewpoint (e.g. turning the head to the side during the video). Given that our patterns for each identity were estimated across multiple different videos of their face, it is unlikely that viewpoint alone could explain the differences between identities. Therefore, our results suggest that the FFA and OFA encode information that relate to face identity, beyond viewpoint.

We note that the lower bounds on the noise ceiling in our analyses were consistently quite low, especially for FFA and pSTS. However, these values are similar to the lower bounds of the noise ceiling in other studies using RSA (e.g. Carlin & Kriegeskorte, 2017; Jozwik et al., 2016; Thornton & Mitchell, 2017; 2018). We considered whether the low correlations could reflect substantial individual differences in face identity brain representations, but our results did not support this possibility. The low noise ceilings in our study likely reflect the fact that the differences between brain-activity patterns associated with faces of different people are small compared to the differences between patterns associated with different visual categories (e.g. faces and places). Moreover, we used identity-based rather than image-based patterns (by crossvalidating across runs presenting different videos for each identity), and this is likely to have introduced additional variability to the pattern estimates. It is also possible that we needed more data per participant, and future studies should consider ways to increase the amount of explainable variance. A related issue is that the perceived-property models had inter-subject reliabilities that varied between .2 and .6 and thus correlations between these models and brain RDMs would be affected by these low reliabilities.

None of the models that we considered here explained the representational geometry of responses in the face-selective right pSTS. It is likely that the pSTS as defined in the present study contains overlapping and interspersed groups of voxels that respond to faces only, voices only, or both faces and voices (Beauchamp et al., 2004) that make the overlapping representational geometry difficult to explain. On the other hand, it is possible that the pSTS represents information about people that we did not consider here, such as idiosyncratic facial movements (Yovel & O'Toole, 2016), emotional and mental states (Thornton et al., 2019), biographical knowledge (Verosky et al., 2013; Collins et al., 2016; Thornton et al., 2019), social distance or network position (Parkinson et al., 2014; 2017), or type of social interactions (Walbrin & Koldewyn, 2019). Future studies may need to explore an even richer set of social, perceptual, and stimulus-based models to better characterise responses in the pSTS (and investigate representations beyond face-selective regions).

A limitation of our study was the lack of diversity of our face identities in terms of race and ethnicity (ten identities were White Caucasian and two were Black), which limits the generalisability of our results to faces of different ethnicities. It was essential to our study that our set of celebrities were highly familiar to our sample of young British participants, and they were chosen based on their recognisability (of both faces and voices — please see Tsantani et al., 2019). Future work will need to incorporate more diversity in the face stimuli. This is also crucial when considering the image-computable models. In particular, OpenFace has been developed, trained, and evaluated on databases that contain large proportions of Caucasian faces when compared to other ethnicities. Future work using larger samples of identities should evaluate the biases caused by these procedures, and develop models trained on more representative and diverse databases.

To conclude, our study highlights the importance of using multiple and diverse representational models to characterise how face identities are represented in different

face-selective regions. Although similar levels of identity decodability were observed in both OFA and FFA (Tsantani et al., 2019), the information explicitly encoded in these two regions is in fact distinct, suggesting that the two regions serve quite different computational roles. Future work attempting to define the computations of cortical regions that appear to serve the same function (e.g. discriminating between identities) would benefit from comparing representations in those regions with multiple and diverse candidate models to reveal the type of information that is encoded.

- 980 Abudarham, N., & Yovel, G. (2016). Reverse engineering the face space:
981 Discovering the critical features for face identification. *Journal of Vision*, 16(3),
982 40-40.
- 983 Abudarham, N., Shkiller, L., & Yovel, G. (2019). Critical features for face
984 recognition. *Cognition*, 182, 73-83.
- 985 Amos, B., Ludwiczuk, B., & Satyanarayanan, M. (2016). Openface: A general-
986 purpose face recognition library with mobile applications. *CMU School of*
987 *Computer Science*, 6, 2.
- 988 Anzellotti, S., & Caramazza, A. (2017). Multimodal representations of person
989 identity individuated with fMRI. *Cortex*, 89, 85-97.
- 990 Anzellotti, S., Fairhall, S. L., & Caramazza, A. (2014). Decoding representations of
991 face identity that are tolerant to rotation. *Cerebral Cortex*, 24(8), 1988–1995.
- 992 Axelrod, V., Rozier, C., Malkinson, T. S., Lehongre, K., Adam, C., Lambrecq, V., ...
993 & Naccache, L. (2019). Face-selective neurons in the vicinity of the human
994 fusiform face area. *Neurology*, 92(4), 197-198.
- 995 Axelrod, V., & Yovel, G. (2012). Hierarchical processing of face viewpoint in
996 human visual cortex. *Journal of Neuroscience*, 32(7), 2442-2452.
- 997 Axelrod, V., & Yovel, G. (2015). Successful decoding of famous faces in the
998 fusiform face area. *PLoS ONE*, 10(2), 19–25.
- 999 Baltrusaitis, T., Zadeh, A., Lim, Y. C., & Morency, L. P. (2018, May). Openface
1000 2.0: Facial behavior analysis toolkit. In *2018 13th IEEE International*
1001 *Conference on Automatic Face & Gesture Recognition (FG 2018)* (pp. 59-66).
1002 IEEE.
- 1003 Beauchamp, M. S., Argall, B. D., Bodurka, J., Duyn, J. H., & Martin, A. (2004).
1004 Unraveling multisensory integration: patchy organization within human STS
1005 multisensory cortex. *Nature neuroscience*, 7(11), 1190-1192.
- 1006 Biederman, I., & Kalocsai, P. (1997). Neurocomputational bases of object and face
1007 recognition. *Philosophical Transactions of the Royal Society of London. Series*
1008 *B: Biological Sciences*, 352(1358), 1203-1219.
- 1009 Calder, A. J., Burton, A. M., Miller, P., Young, A. W., & Akamatsu, S. (2001). A
1010 principal component analysis of facial expressions. *Vision research*, 41(9),
1011 1179-1208.
- 1012 Carlin, J. D., & Kriegeskorte, N. (2017). Adjudicating between face-coding models
1013 with individual-face fMRI responses. *PLoS computational biology*, 13(7),
1014 e1005604.
- 1015 Collins, J. A., Koski, J. E., & Olson, I. R. (2016). More than meets the eye: The
1016 merging of perceptual and conceptual knowledge in the anterior temporal face
1017 area. *Frontiers in human neuroscience*, 10, 189.
- 1018 Davidesco, I., Zion-Golumbic, E., Bickel, S., Harel, M., Groppe, D. M., Keller, C. J.,
1019 ... & Schroeder, C. E. (2014). Exemplar selectivity reflects perceptual
1020 similarities in the human fusiform cortex. *Cerebral cortex*, 24(7), 1879-1893.

- di Oleggio Castello, M. V., Halchenko, Y. O., Guntupalli, J. S., Gors, J. D., & Gobbini, M. I. (2017). The neural representation of personally familiar and unfamiliar faces in the distributed system for face perception. *Scientific reports*, 7(1), 1-14.
- Dubois, J., de Berker, A. O., & Tsao, D. Y. (2015). Single-unit recordings in the macaque face patch system reveal limitations of fMRI MVPA. *Journal of Neuroscience*, 35(6), 2791-2802.
- Duchaine, B., & Yovel, G. (2015). A revised neural framework for face processing. *Annual Review of Vision Science*, 1, 393-416.
- Fedorenko, E., Hsieh, P. J., Nieto-Castañón, A., Whitfield-Gabrieli, S., & Kanwisher, N. (2010). New method for fMRI investigations of language: defining ROIs functionally in individual subjects. *Journal of neurophysiology*, 104(2), 1177-1194.
- Ghuman, A. S., Brunet, N. M., Li, Y., Konecky, R. O., Pyles, J. A., Walls, S. A., ... & Richardson, R. M. (2014). Dynamic encoding of face information in the human fusiform gyrus. *Nature communications*, 5(1), 1-10.
- Goesaert, E., & de Beeck, H. P. O. (2013). Representations of facial identity information in the ventral visual stream investigated with multivoxel pattern analyses. *Journal of Neuroscience*, 33(19), 8549-8558.
- Grill-Spector, K., Kushnir, T., Edelman, S., Avidan, G., Itzhak, Y., & Malach, R. (1999). Differential processing of objects under various viewing conditions in the human lateral occipital complex. *Neuron*, 24(1), 187-203.
- Grossman, S., Gaziv, G., Yeagle, E. M., Harel, M., Mégevand, P., Groppe, D. M., ... & Malach, R. (2019). Convergent evolution of face spaces across human face-selective neuronal groups and deep convolutional networks. *Nature communications*, 10(1), 1-13.
- Guntupalli, J. S., Wheeler, K. G., & Gobbini, M. I. (2017). Disentangling the representation of identity from head view along the human face processing pathway. *Cerebral Cortex*, 27(1), 46-53.
- Haxby, J. V., Hoffman, E. A., & Gobbini, M. I. (2000). The distributed human neural system for face perception. *Trends in cognitive sciences*, 4(6), 223-233.
- Jenkins, R., White, D., Van Montfort, X., & Burton, A. M. (2011). Variability in photos of the same face. *Cognition*, 121(3), 313-323.
- Julian, J. B., Fedorenko, E., Webster, J., & Kanwisher, N. (2012). An algorithmic method for functionally defining regions of interest in the ventral visual pathway. *Neuroimage*, 60(4), 2357-2364.
- Jozwik, K. M., Kriegeskorte, N., & Mur, M. (2016). Visual features as stepping stones toward semantics: Explaining object similarity in IT and perception with non-negative least squares. *Neuropsychologia*, 83, 201-226.
- Jozwik, K. M., Kriegeskorte, N., Storrs, K. R., & Mur, M. (2017). Deep convolutional neural networks outperform feature-based but not categorical models in explaining object similarity judgments. *Frontiers in psychology*, 8, 1726.

- Kanwisher, N., McDermott, J., & Chun, M. M. (1997). The fusiform face area: a module in human extrastriate cortex specialized for face perception. *The Journal of Neuroscience*, 17(11), 4302–11.
- Khaligh-Razavi, S. M., & Kriegeskorte, N. (2014). Deep supervised, but not unsupervised, models may explain IT cortical representation. *PLoS computational biology*, 10(11).
- Khuvis, S., Yeagle, E. M., Norman, Y., Grossman, S., Malach, R., & Mehta, A. D. (2018). Face-selective units in human ventral temporal cortex reactivate during free recall. *BioRxiv*, 487686.
- Kietzmann, T. C., Swisher, J. D., König, P., & Tong, F. (2012). Prevalence of selectivity for mirror-symmetric views of faces in the ventral and dorsal visual pathways. *Journal of Neuroscience*, 32(34), 11763-11772.
- Kriegeskorte, N., Mur, M., Ruff, D. A., Kiani, R., Bodurka, J., Esteky, H., ... & Bandettini, P. A. (2008a). Matching categorical object representations in inferior temporal cortex of man and monkey. *Neuron*, 60(6), 1126-1141.
- Kriegeskorte, N., Mur, M., & Bandettini, P. (2008b). Representational similarity analysis - connecting the branches of systems neuroscience. *Frontiers in Systems Neuroscience*, 2, 1–28.
- Margalit, E., Biederman, I., Herald, S. B., Yue, X., & von der Malsburg, C. (2016). An applet for the Gabor similarity scaling of the differences between complex stimuli. *Attention, Perception, & Psychophysics*, 78(8), 2298-2306.
- McKone, E., Brewer, J. L., MacPherson, S., Rhodes, G., & Hayward, W. G. (2007). Familiar other-race faces show normal holistic processing and are robust to perceptual stress. *Perception*, 36(2), 224-248.
- Nestor, A., Plaut, D. C., & Behrmann, M. (2011). Unraveling the distributed neural code of facial identity through spatiotemporal pattern analysis. *Proceedings of the National Academy of Sciences of the United States of America*, 108(24), 9998–10003.
- Nili, H., Wingfield, C., Walther, A., Su, L., Marslen-Wilson, W., & Kriegeskorte, N. (2014). A Toolbox for Representational Similarity Analysis. *PLoS Computational Biology*, 10(4). <http://doi.org/10.1371/journal.pcbi.1003553>
- Oliva, A., & Torralba, A. (2001). Modeling the shape of the scene: A holistic representation of the spatial envelope. *International journal of computer vision*, 42(3), 145-175.
- Oosterhof, N. N., & Todorov, A. (2008). The functional basis of face evaluation. *Proceedings of the National Academy of Sciences*, 105(32), 11087-11092.
- Parkinson, C., Kleinbaum, A. M., & Wheatley, T. (2017). Spontaneous neural encoding of social network position. *Nature Human Behaviour*, 1(5), 1-7.
- Parkinson, C., Liu, S., & Wheatley, T. (2014). A common cortical metric for spatial, temporal, and social distance. *Journal of Neuroscience*, 34(5), 1979-1987.
- Pitcher, D., Dilks, D. D., Saxe, R. R., Triantafyllou, C., & Kanwisher, N. (2011). Differential selectivity for dynamic versus static information in face-selective cortical regions. *Neuroimage*, 56(4), 2356-2363.

1107 Ramírez, F. M., Cichy, R. M., Allefeld, C., & Haynes, J. D. (2014). The neural code
1108 for face orientation in the human fusiform face area. *Journal of*
1109 *Neuroscience*, 34(36), 12155-12167.

1110 Rhodes, G. (1988). Looking at faces: First-order and second-order features as
1111 determinants of facial appearance. *Perception*, 17(1), 43-63.

1112 Rossion, B., Hanseeuw, B., & Dricot, L. (2012). Defining face perception areas in
1113 the human brain: a large-scale factorial fMRI face localizer analysis. *Brain and*
1114 *cognition*, 79(2), 138-157.

1115 Russell, R., Biederman, I., Nederhouser, M., & Sinha, P. (2007). The utility of
1116 surface reflectance for the recognition of upright and inverted faces. *Vision*
1117 *research*, 47(2), 157-165.

1118 Russell, R., & Sinha, P. (2007). Real-world face recognition: The importance of
1119 surface reflectance properties. *Perception*, 36(9), 1368-1374.

1120 Storrs, K. Khaligh-Razavi, S. & Kriegeskorte, N. (2020). Noise ceiling on the
1121 crossvalidated performance of reweighted models of representational
1122 dissimilarity: Addendum to Khaligh-Razavi & Kriegeskorte (2014). *bioRxiv*. doi:
1123 <https://doi.org/10.1101/2020.03.23.003046>

1124 Sutherland, C. A., Oldmeadow, J. A., Santos, I. M., Towler, J., Burt, D. M., &
1125 Young, A. W. (2013). Social inferences from faces: Ambient images generate
1126 a three-dimensional model. *Cognition*, 127(1), 105-118.

1127 Tardif, J., Morin Duchesne, X., Cohan, S., Royer, J., Blais, C., Fiset, D., ... &
1128 Gosselin, F. (2019). Use of face information varies systematically from
1129 developmental prosopagnosics to super-recognizers. *Psychological Science*,
1130 30(2), 300-308.

1131 Thornton, M. A., & Mitchell, J. P. (2017). Consistent neural activity patterns
1132 represent personally familiar people. *Journal of cognitive neuroscience*, 29(9),
1133 1583-1594.

1134 Thornton, M. A., & Mitchell, J. P. (2018). Theories of person perception predict
1135 patterns of neural activity during mentalizing. *Cerebral cortex*, 28(10), 3505-
1136 3520.

1137 Thornton, M., Weaverdyck, M., & Tamir, D. (2019). The brain represents people
1138 as the mental states they habitually experience. *Nature Communications*, 10,
1139 2291.

1140 Tsantani, M., Kriegeskorte, N., McGettigan, C., & Garrido, L. (2019). Faces and
1141 voices in the brain: a modality-general person-identity representation in
1142 superior temporal sulcus. *Neuroimage*, 201, 116004.

1143 Verosky, S. C., Todorov, A., & Turk-Browne, N. B. (2013). Representations of
1144 individuals in ventral temporal cortex defined by faces and biographies.
1145 *Neuropsychologia*, 51(11), 2100–2108.

1146 Walbrin, J., & Koldewyn, K. (2019). Dyadic interaction processing in the posterior
1147 temporal cortex. *NeuroImage*, 198, 296-302.

1148 Walther, A., Nili, H., Ejaz, N., Alink, A., Kriegeskorte, N., & Diedrichsen, J. (2016).
1149 Reliability of dissimilarity measures for multi-voxel pattern analysis.

1150 *NeuroImage*, 137(0), 188–200.
 1151 <http://doi.org/10.1016/j.neuroimage.2015.12.012>
 1152 Weibert, K., Flack, T. R., Young, A. W., & Andrews, T. J. (2018). Patterns of
 1153 neural response in face regions are predicted by low-level image properties.
 1154 *Cortex*, 103, 199-210.
 1155 Yovel, G., & Duchaine, B. (2006). Specialized face perception mechanisms extract
 1156 both part and spacing information: Evidence from developmental
 1157 prosopagnosia. *Journal of Cognitive Neuroscience*, 18(4), 580-593.
 1158 Yovel, G., & O'Toole, A. J. (2016). Recognizing people in motion. *Trends in*
 1159 *cognitive sciences*, 20(5), 383-395.
 1160 Yue, X., Biederman, I., Mangini, M. C., Malsburg, C. von der, & Amir, O. (2012).
 1161 Predicting the psychophysical similarity of faces and non-face complex shapes
 1162 by image-based measures. *Vision Research*, 55, 41–46.
 1163 Zhang, H., Japee, S., Nolan, R., Chu, C., Liu, N., & Ungerleider, L. (2016). Face-
 1164 selective regions differ in their ability to classify facial expressions.
 1165 *Neuroimage*, 130, 77-90.
 1166 Zhou, X., & Mondloch, C. J. (2016). Recognizing “Bella Swan” and “Hermione
 1167 Granger”: No own-race advantage in recognizing photos of famous
 1168 faces. *Perception*, 45(12), 1426-1429.
 1169
 1170
 1171
 1172
 1173
 1174
 1175
 1176
 1177
 1178
 1179
 1180
 1181
 1182
 1183
 1184
 1185
 1186
 1187
 1188
 1189
 1190
 1191
 1192
 1193
 1194
 1195
 1196

1197 Tables

1198 **Table 1: Results of individual model analysis.** The values in this table correspond to the results presented
 1199 in Figure 3A. For each ROI, we show the mean correlations between brain RDMs with each model, standard
 1200 error (SE), Z statistics from two-sided one-sample Wilcoxon signed-rank tests, and whether correlations
 1201 were significantly higher than zero. We also show the estimated lower and upper bounds of the noise ceiling
 1202 for each ROI. Models are ordered by effect size.

		Pearson correlation between RDMs				Noise ceiling
		Mean <i>r</i>	<i>SE</i>	<i>Z</i>	<i>p</i> < .05 (FDR corrected)	[Lower bound Upper bound]
rFFA						[0.135 0.262]
	Perceived Similarity	0.109	0.023	3.689	yes	
	Social Traits (All)	0.104	0.031	2.710	yes	
	Open Face	0.101	0.023	3.461	yes	
	Attractiveness	0.090	0.033	2.687	yes	
	Gender	0.086	0.021	3.302	yes	
	Valence	0.060	0.023	2.391	yes	
	Dominance	0.058	0.030	1.640	no	
	Gabor-Jet	0.052	0.049	0.956	no	
	Trustworthiness	0.040	0.029	1.594	no	
	Pixel-Faces	0.035	0.044	0.865	no	
	Pixel-Frames	0.005	0.027	0.159	no	
	GIST-Faces	-0.006	0.040	0.114	no	
	Pixel-Frames	-0.018	0.041	-0.478	no	
rOFA						[0.337 0.408]
	Pixel-Faces	0.221	0.031	4.357	yes	
	Gabor-Jet	0.204	0.037	3.968	yes	
	Pixel-Frames	0.107	0.031	3.016	yes	
	GIST-Faces	0.104	0.043	2.216	yes	
	Attractiveness	0.092	0.029	2.843	yes	
	Social Traits (All)	0.083	0.031	1.979	no	
	Gender	0.074	0.021	2.757	yes	
	OpenFace	0.067	0.020	2.952	yes	

	Dominance	0.055	0.031	1.546	no
	Perceived Similarity	0.039	0.026	1.416	no
	GIST-Frames	0.025	0.034	0.746	no
	Trustworthiness	0.011	0.025	0.400	no
	Valence	-0.016	0.031	-0.573	no
<hr/>					
rpSTS					[0.126 0.252]
	GIST-Frames	0.075	0.047	1.800	no
	Dominance	0.052	0.027	1.800	no
	OpenFace	0.040	0.020	2.129	no
	Social Traits (All)	0.032	0.026	1.018	no
	Pixel-Frames	0.022	0.030	0.956	no
	Gender	0.020	0.017	0.956	no
	Trustworthiness	0.017	0.032	0.524	no
	Attractiveness	0.005	0.024	0.134	no
	Valence	0.002	0.031	0.051	no
	Pixel-Faces	-0.003	0.035	-0.113	no
	Perceived Similarity	-0.008	0.026	-0.072	no
	Gabor-Jet	-0.045	0.040	-1.100	no
	GIST-Faces	-0.048	0.036	-1.368	no

Table 2: Results of weighted representational modelling analysis. The values in this table correspond to the results presented in Figure 3B. Within each ROI, we show the mean correlations between brain RDMS with each model (individual models and combined models), and whether correlations were significantly higher than zero. We also show the estimated lower and upper bounds of the noise ceiling for each ROI, and whether correlations were significantly below the noise ceiling. Models are ordered by effect size and grouped first by image-computable models, then perceived-property models, and then models that combined both types of properties. RW refers to combined and reweighted models.

	Pearson correlation between RDMS			Noise ceiling	
	Mean <i>r</i>	<i>SE</i>	<i>p</i> < .05 (Bonferroni corrected)	[Lower bound Upper bound]	<i>p</i> < .05 (Bonferroni corrected)
rFFA				[0.089 0.286]	
	Open Face	0.105	0.032	yes	no
	Gabor-Jet	0.041	0.042	no	no

	Pixel-Faces	0.027	0.040	no	no
	Pixel-Frames	0.019	0.036	no	no
	GIST-Faces	0.007	0.037	no	no
	GIST-Frames	-0.010	0.037	no	no
	RW Image-Computable	0.063	0.037	no	no
	Perceived Similarity	0.118	0.031	yes	no
	Social Traits (All)	0.102	0.035	yes	no
	Gender	0.094	0.033	yes	no
	Attractiveness	0.091	0.035	no	no
	Valence	0.059	0.031	no	no
	Trustworthiness	0.049	0.033	no	no
	Dominance	0.048	0.034	no	no
	RW Social Traits	0.074	0.034	no	no
	RW Perceived	0.100	0.033	yes	no
	RW Low-Level	-0.006	0.035	no	no
	RW High-Level	0.096	0.033	yes	no
	RW ALL	0.086	0.035	no	no
<hr/>					
rOFA					[0.237 0.372]
	Pixel-Faces	0.158	0.041	yes	no
	Gabor-Jet	0.138	0.047	yes	no
	Pixel-Frames	0.108	0.039	no	yes
	GIST-Faces	0.087	0.047	no	no
	OpenFace	0.066	0.041	no	yes
	GIST-Frames	0.050	0.042	no	yes
	RW Image Computable	0.089	0.044	no	no
	Gender	0.082	0.041	no	no
	Attractiveness	0.075	0.039	no	yes
	Social Traits (All)	0.067	0.040	no	yes
	Perceived Similarity	0.055	0.039	no	yes
	Dominance	0.039	0.038	no	yes

Trustworthiness	0.031	0.040	no	yes
Valence	-0.010	0.041	no	yes
RW Social Traits	0.037	0.040	no	yes
RW Perceived	0.033	0.040	no	yes
RW Low-Level	0.103	0.046	no	no
RW High-Level	0.019	0.040	no	yes
RW ALL	0.059	0.041	no	yes
rpSTS				[0.091 0.277]
GIST-Frames	0.051	0.040	no	no
OpenFace	0.034	0.030	no	no
Pixel-Faces	0.009	0.034	no	no
Pixel-Frames	0.006	0.032	no	no
GIST-Faces	-0.031	0.034	no	no
Gabor-Jet	-0.038	0.037	no	no
RW Image- Computable	0.013	0.036	no	no
Dominance	0.054	0.030	no	no
Social Traits (All)	0.035	0.030	no	no
Trustworthiness	0.026	0.033	no	no
Gender	0.023	0.029	no	no
Valence	0.005	0.033	no	no
Attractiveness	0.003	0.029	no	no
Perceived Similarity	-0.003	0.032	no	no
RW Social Traits	0.026	0.033	no	no
RW Perceived	0.031	0.032	no	no
RW Low-Level	0.010	0.038	no	no
RW High-Level	0.033	0.031	no	no
RW ALL	0.025	0.030	no	no

1214

1215

1216

1217

1218

Figure captions

Figure 1. Examples of face trials in the fMRI and behavioural experiments. All experiments presented the same videos of moving, non-speaking, faces of 12 famous people. For each famous person, we presented six naturalistically varying videos of their face. In an event-related fMRI task, each trial presented a single face video. This task also contained trials of the same length featuring voice clips (excluded from the present analysis), stimuli relating to the anomaly detection task, and fixation (null events). In each trial of the Social Trait Judgements Tasks (separate tasks for Trustworthiness, Dominance, Attractiveness, and Valence), participants viewed three videos of the face of the same identity and judged the intensity of the target trait (on a scale from 1 to 7). In each trial of the Perceived Similarity Task, participants viewed three videos of one identity followed by three videos of a different identity and rated their visual similarity (from 1 to 7). Face videos were presented for their full duration of 3000ms in the fMRI experiment, whereas only the first 1500ms were presented in the behavioural experiments.

Figure 2. Brain and model representational dissimilarity matrices (RDMs). **A:** Location in MNI space of the three face-selective regions localised in our participants: OFA (occipital face area), FFA (fusiform face area), and pSTS (posterior superior temporal sulcus; all regions in the right hemisphere). These probabilistic maps were created for illustration purposes (in our analyses, we only used subject-specific regions of interest (ROIs)) and show all voxels that were present in at least 20% of participants. **B:** Example brain representational dissimilarity matrix (RDM) for the right FFA. For each ROI and each participant, we computed RDMs showing the dissimilarity of the brain response patterns between all pairs of identities. Each row and column represent one identity, and response patterns are based on all six presented videos of that identity. Each cell shows the linear discriminant contrast distance between the response patterns of two identities (higher values indicate higher dissimilarity), crossvalidated across runs presenting different videos of the face of each identity. The matrix is symmetric around a diagonal of zeros. **C:** Model RDMs for *image-computable properties* (blue) and *perceived properties* (pink). These models are in the same format as the brain RDMs and show the dissimilarity between two identities on each property (see Methods). *Image-computable models* include a neural network trained to distinguish between face identities (OpenFace), a Gabor-Jet model, Pixel Dissimilarity (both for faces only — Pixel-Faces, and the whole frames — Pixel-Frames), and a GIST Descriptor model (both for faces — GIST-Faces, and the whole frames — GIST-Frames). The RDMs computed per image (before averaging across identity) are shown in Extended Data Figure 2-1, though those 72x72 RDMs were not used in any analysis. *Perceived-property models* include perceived social traits (Trustworthiness, Dominance, Attractiveness, Valence, Social Traits (All)), Perceived Similarity, and Gender. Models based on participant ratings were averaged across participants. All models were built based on multiple images (image-computable models) or videos (perceived-property models) of the face of each identity. For visualisation purposes, all model RDMs were scaled to a range between zero (no dissimilarity) and one (maximum dissimilarity). **D:** Correlations (Pearson) between the different model RDMs. The different candidate models were compared with each other using Pearson correlation. Extended Data Figure 2-2 shows this same matrix with added correlation values.

Figure 3. FFA and OFA show distinct representational profiles of face identity information. A: Similarity (Pearson correlations) between brain RDMs (in FFA, OFA, and pSTS) and each of the individual candidate models. Bars show mean correlations across participants and error bars show standard error. Correlations with image-computable models are in blue and with perceived-property models are in pink. Horizontal dashed lines show the lower bound of the noise ceiling. An asterisk above a bar and the name of the model in bold indicate that correlations with that model were significantly higher than zero. Correlations with individual models are sorted from highest to lowest. Horizontal lines above bars show significant differences between the correlations of the first marked column with the subsequent marked columns (FDR corrected for multiple comparisons). [Full results are Table 1, and single-subject data are shown in Figure 4.](#) **B: Similarity (Pearson correlations) between brain RDMs (in FFA, OFA, and pSTS) and each of the candidate models in the weighted representational modelling analysis.** Bars show mean correlations and error bars show standard error across 1,000 bootstrap samples. Horizontal dashed lines show the lower bound of the noise ceiling, averaged across bootstrap samples. An asterisk above a bar and the name of the model in bold indicate that correlations with that model were significantly higher than zero. Correlations with individual models are blocked by type of model (image-computable models followed by perceived-property models) and sorted from highest to lowest. RW shows the combined and reweighted models and appears in light blue for models that combine image-computable properties, in light pink for models that combine perceived properties, and in grey for models that combine both types of properties. None of the combined models outperformed individual models. [Full results are reported in Table 2.](#) The results of both analyses show that in the FFA, the models that explained most of the variance are related to high-level properties, such as perceived properties of the stimuli and the image-computable OpenFace model of face recognition. In contrast, brain RDMs in OFA correlated mainly with low-level image-computable properties such as pixel dissimilarity and the Gabor-Jet model. No significant correlations were found in pSTS.

Figure 4. Similarity between brain RDMs (in FFA, OFA, and pSTS) and each of the candidate models, showing individual participant data. This figure shows the same data as Figure 3A, but with added individual data. Circles show correlations for individual participants. Coloured lines show mean (full lines) and median (dotted lines) correlations across participants. Correlations with models based on perceived-property models are in pink, and correlations with image-computable models are in blue. Horizontal black dotted lines mark the zero correlation point. An asterisk above a bar and the name of the model in bold indicate correlations that were significantly higher than zero. Correlations with individual models are sorted from highest to lowest based on the mean correlation across participants to match the format of Figure 3A.

Figure 5. Control analyses with modified model RDMs. A: Similarity between brain RDMs (in FFA, OFA, and pSTS) and each of the candidate models, using image-computable models derived from 72 images per video. Our main analysis in Figure 3A used a single image per video to compute image-computable models. Here, we repeated all analyses of image-computable models using 72 frames for each video. We extracted

72 image frames for each video, and applied each model to each image. For each model, after extracting the features of each image of each video, we averaged the values for all images belonging to the same video. We then computed distances between videos in the same manner as before, and averaged distances for each pair of identities. We note that these results were very similar to the ones using just with one image per video, but some correlations were lower. **B: Similarity between brain RDMs (in FFA, OFA, and pSTS) and each of the individual candidate models, using behavioural models based on individual participant ratings.** The analysis was the same as in Figure 3A, but instead of using average behavioural RDMs, each participant's brain RDM was correlated to their own behavioural RDMs for Perceived Similarity, Trustworthiness, Dominance, Attractiveness, Valence, and Social Traits (All). The pattern of results looked very similar to the ones in Figure 3A, but correlations with perceived-property models were overall lower when using each participant's own model RDMs.

Figure 6. Control analyses using other similarity measures between RDMs. Similarity between brain RDMs (in FFA, OFA, and pSTS) and each of the candidate models using Spearman correlation (A) and Kendall tau-a (B). These analyses were identical to the analysis using Pearson correlations (Figure 3A), with the exception that noise ceiling was computed after rank-transforming the RDMs (Nili et al., 2014). The pattern of results was similar across all three correlation measures.

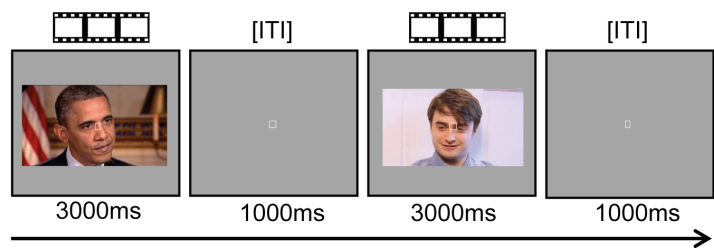
Figure 7. Control analysis with modified brain RDMs. Similarity between brain RDMs for voices (in FFA, OFA, and pSTS) and each of the candidate models for faces. We computed representational dissimilarity matrices (RDMs) from response patterns to voices in the rFFA, rOFA, and rpSTS, and compared them with our model RDMs for faces (same models as in Figure 2). The voice stimuli belonged to the same 12 identities as the face stimuli and were presented interspersed among the face videos in the same runs (see Methods section). RDMs for voice identities were computed using the same procedure as for face identities (see Methods section) and were compared to model RDMs for faces using Pearson correlation. Correlations with individual models are sorted from highest to lowest. None of the correlations were significantly greater than zero after correction for multiple comparisons. Pairwise comparisons showed no significant differences between the correlations of any pairs of models.

Figure 2-1. Image-computable model representational dissimilarity matrices (RDMs) per image. Model RDMs computed from dissimilarities between images for OpenFace, Gabor-Jet, Pixel-Faces, Pixel-Frames, GIST-Faces, and GIST-Frames. Each row/column represents a single image, and images are clustered by identity (6 images for each of the 12 identities). Each cell shows the dissimilarity between the two images in the corresponding rows and columns, with a value of zero indicating that images are identical. Matrices are symmetric around a diagonal of zeros. From these models, only the OpenFace model grouped different images of the same identity as more similar compared to images from different identities. [Please note that these full RDMs were not used in any analysis. Instead, we created 12x12 RDMs \(one entry for each of the 12 identities\) to be](#)

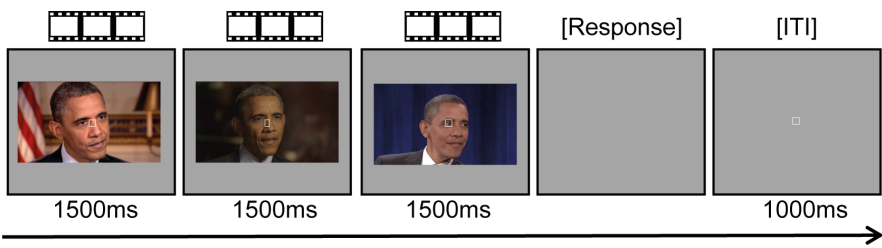
comparable to the brain RDMs (Figure 2C). To create the 12x12 RDMs, we computed the mean of all cells that showed images of the same identity pair.

Figure 2-2. Correlations (Pearson) between the different model RDMs. The different candidate models were compared with each other using Pearson correlation. This is the same figure as 2D, but with added correlation values for each cell.

fMRI



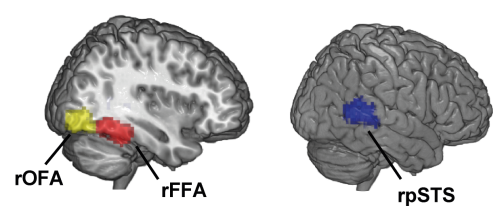
Social Trait Judgements



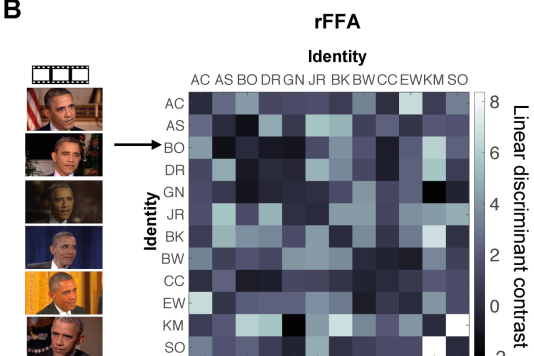
Perceived Similarity



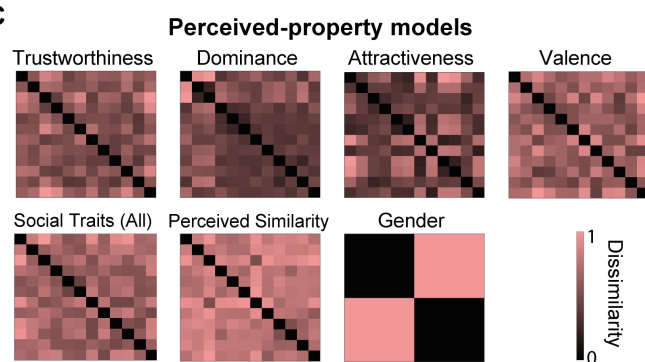
A



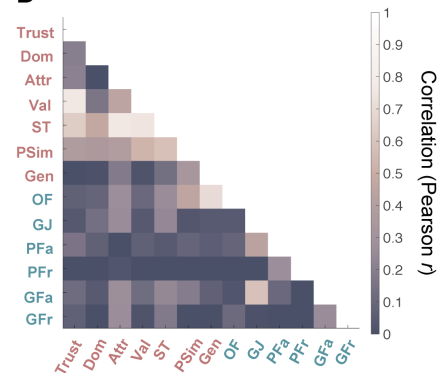
B



C

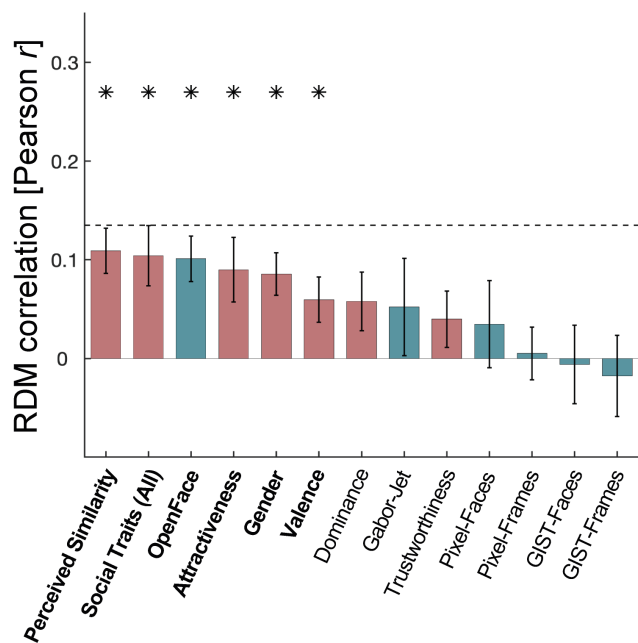


D

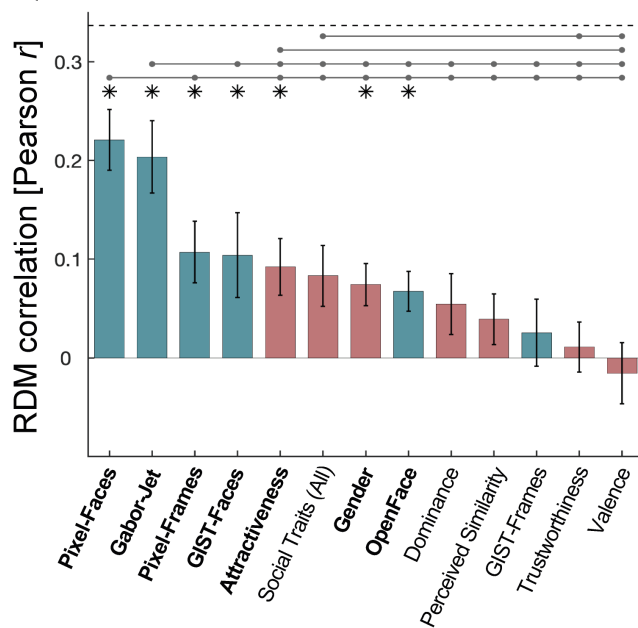


A. Individual model analysis

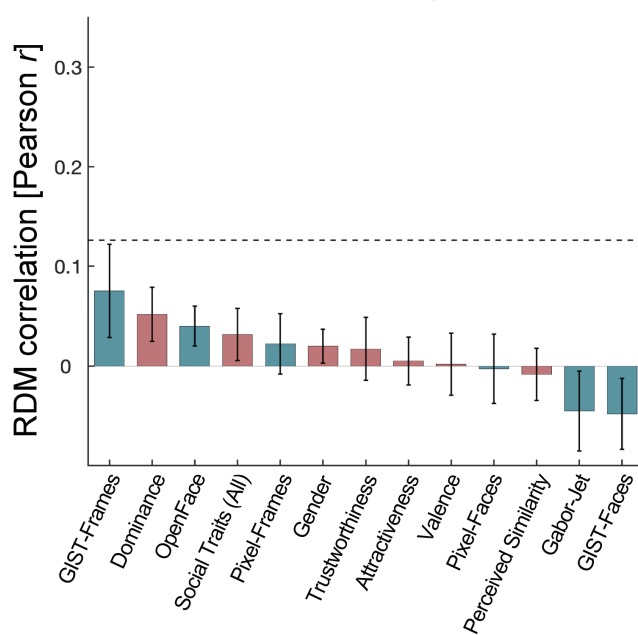
rFFA



rOFA



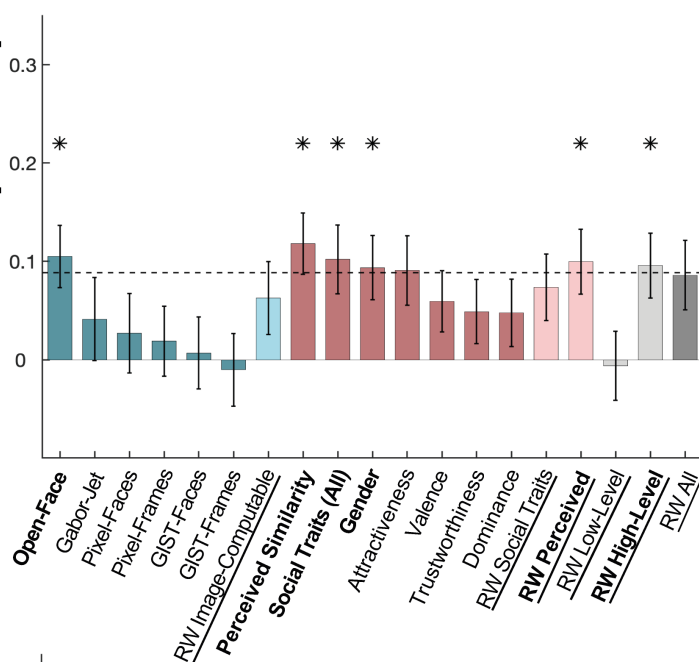
rpSTS



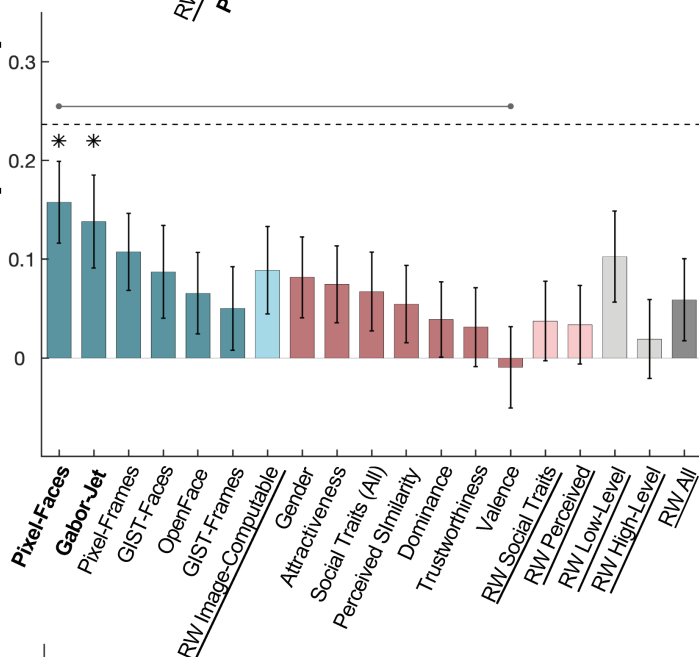
Perceived-property models Image-computable models

B. Weighted model-combination analysis

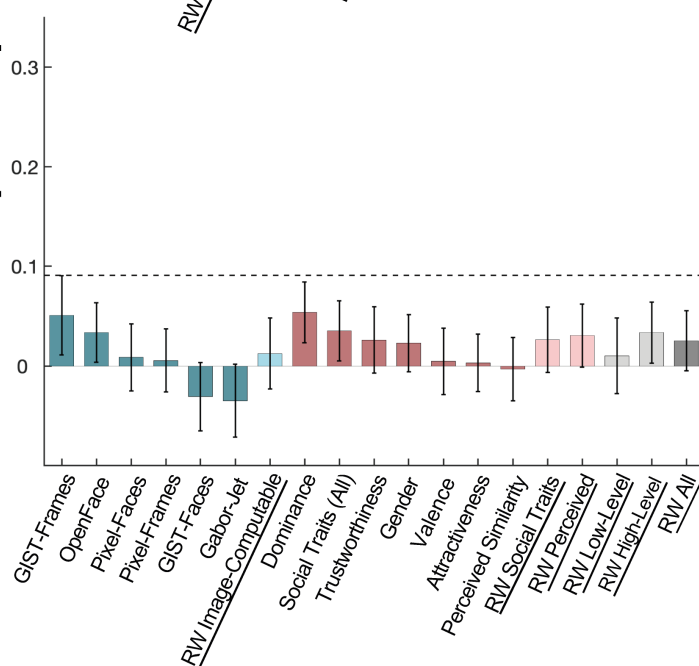
RDM correlation [Pearson r]



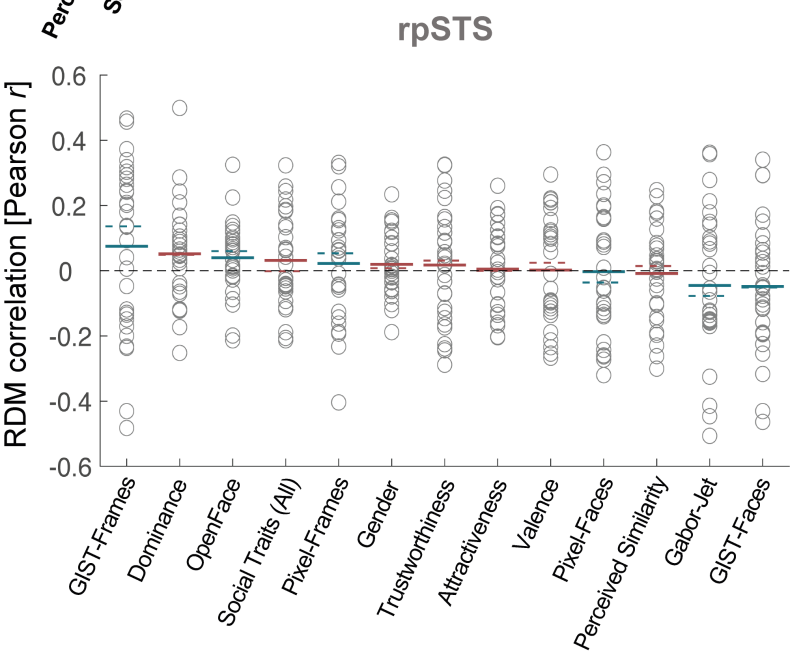
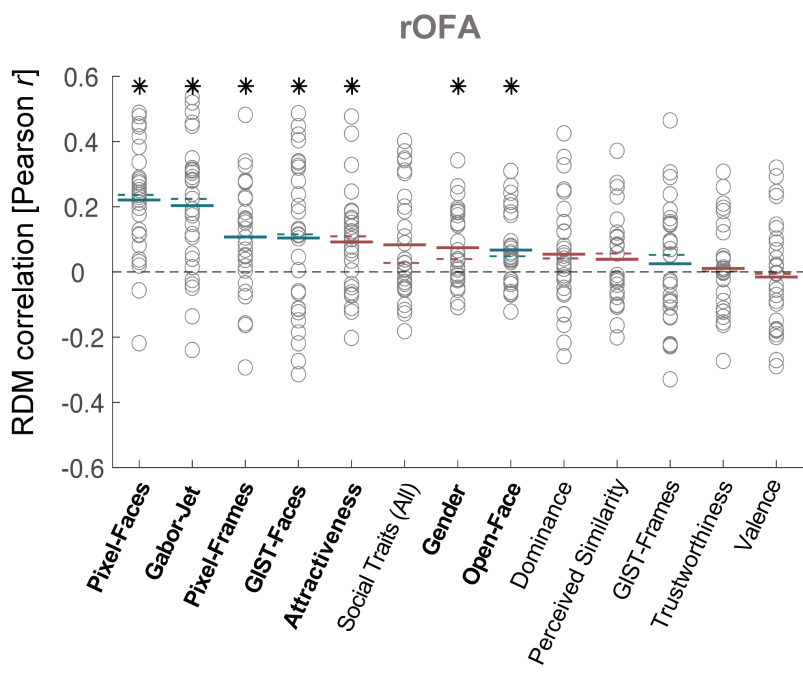
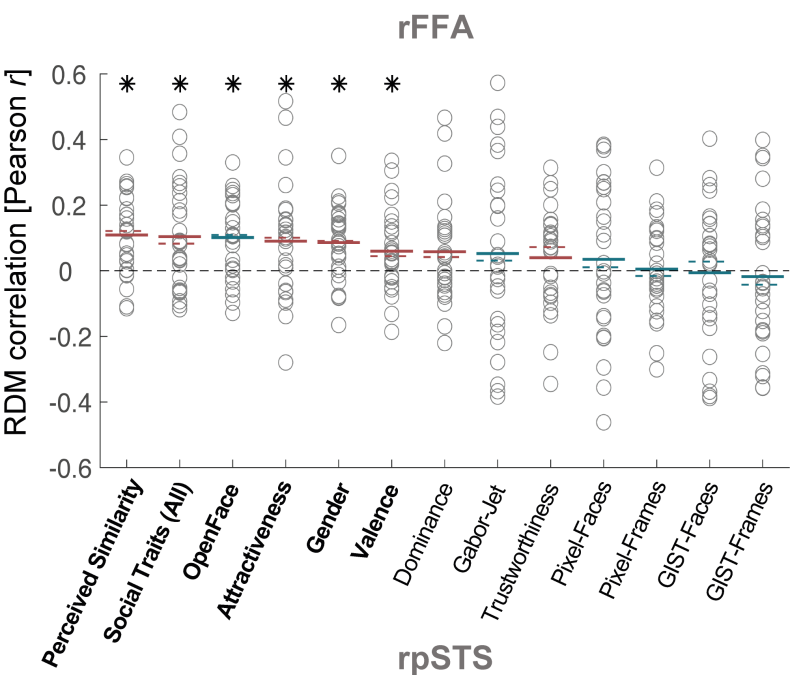
RDM correlation [Pearson r]



RDM correlation [Pearson r]



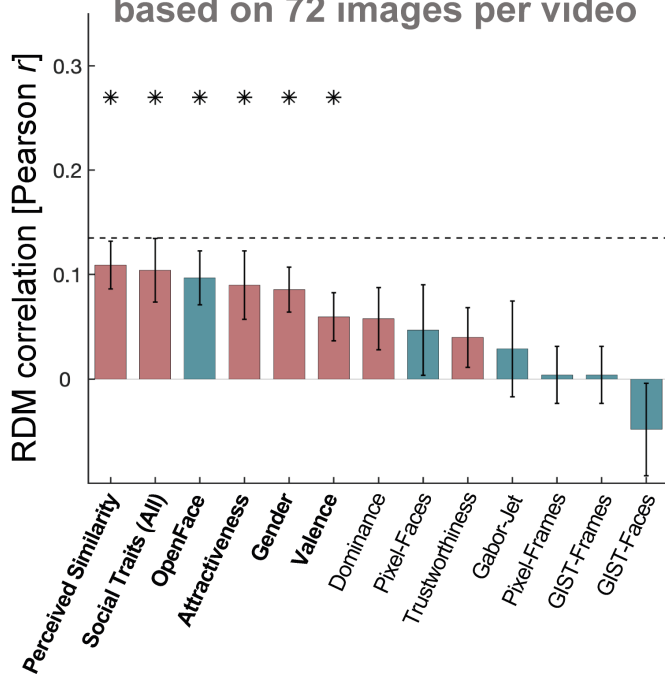
Combined perceived-property Combined image-computable
Combined Low- or High-Level Combined ALL



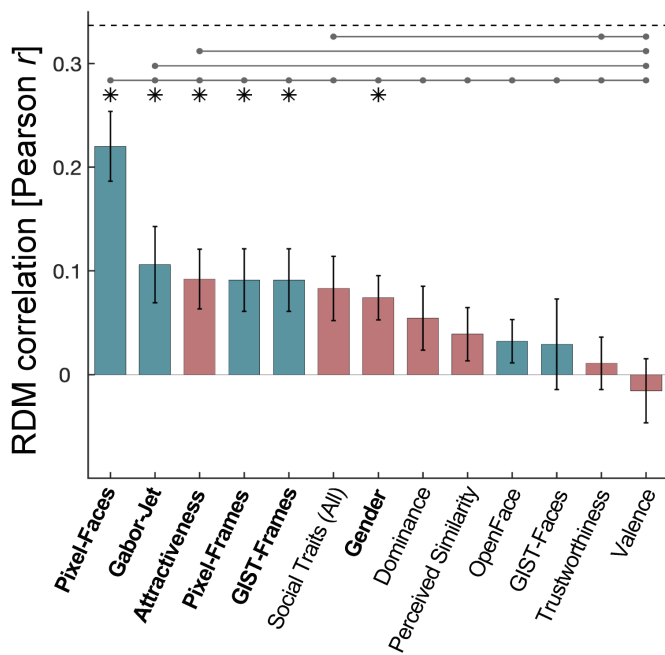
Perceived-property models Image-computable models

A. Image-computable models based on 72 images per video

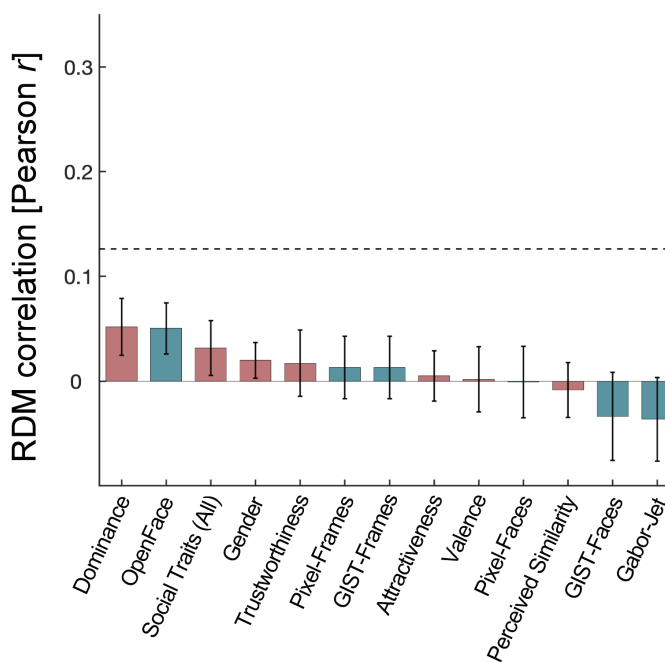
rFFA



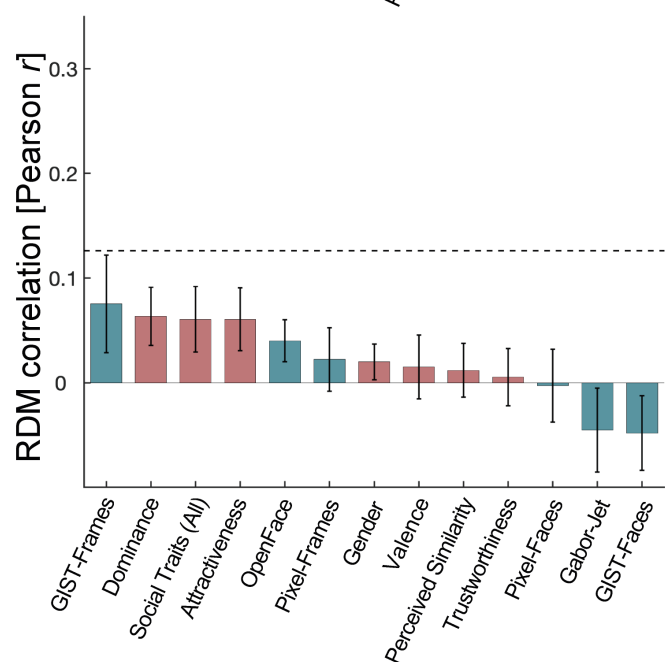
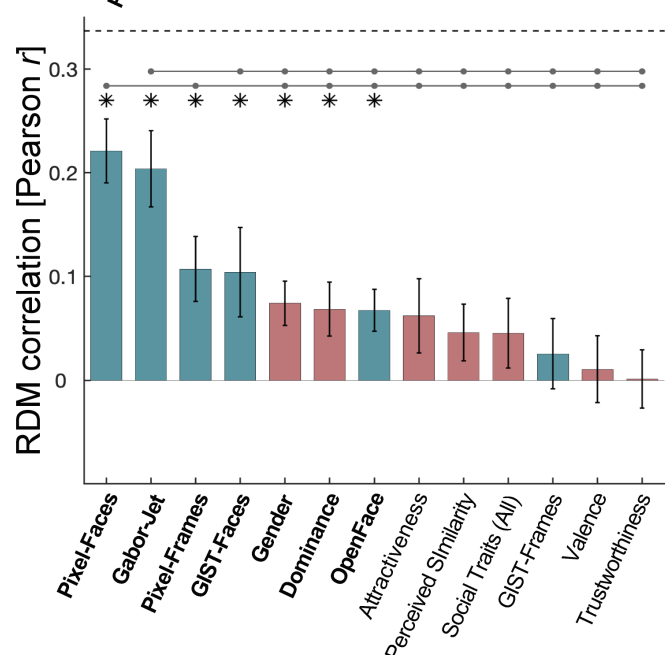
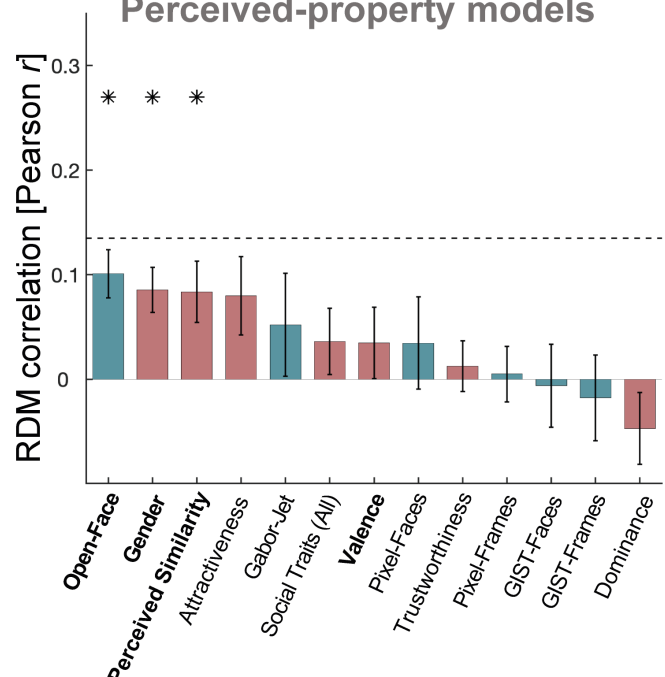
rOFA



rpSTS



B. Participant specific Perceived-property models

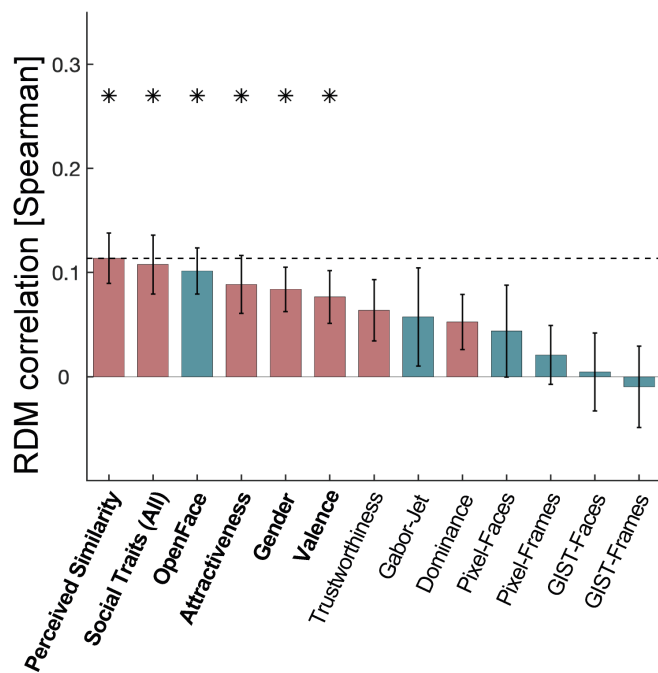


Perceived-property models

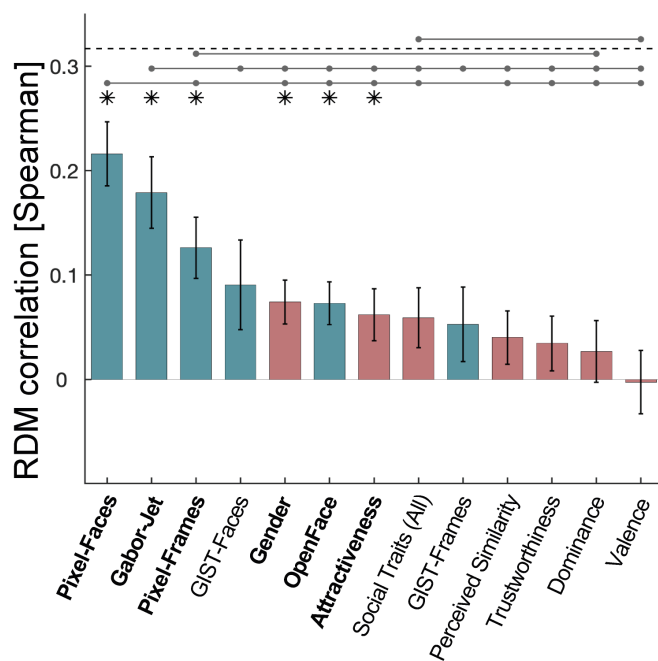
Image-computable models

A. Spearman

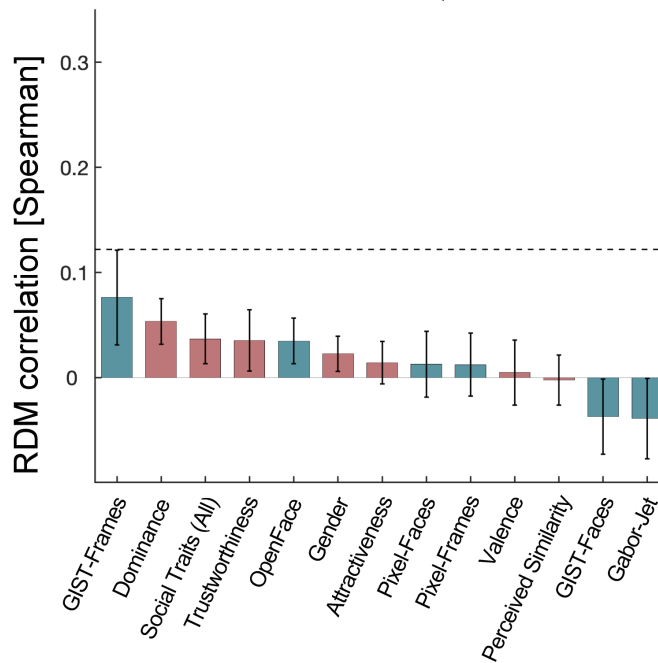
rFFA



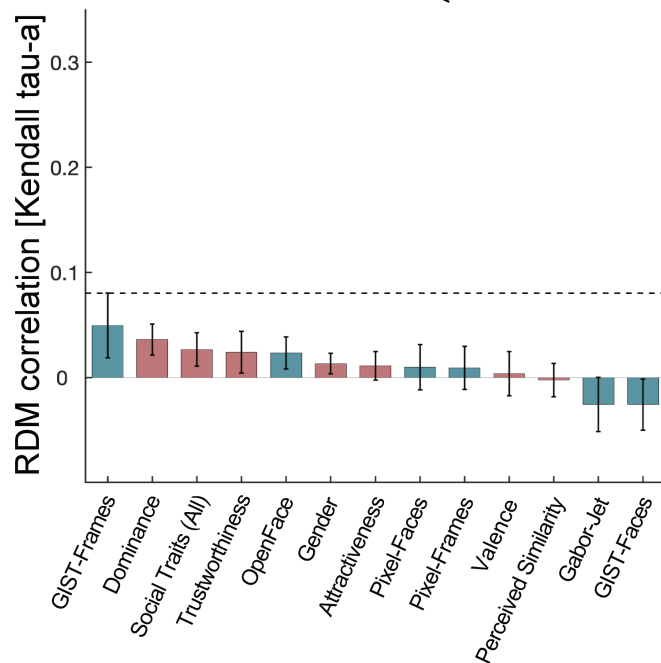
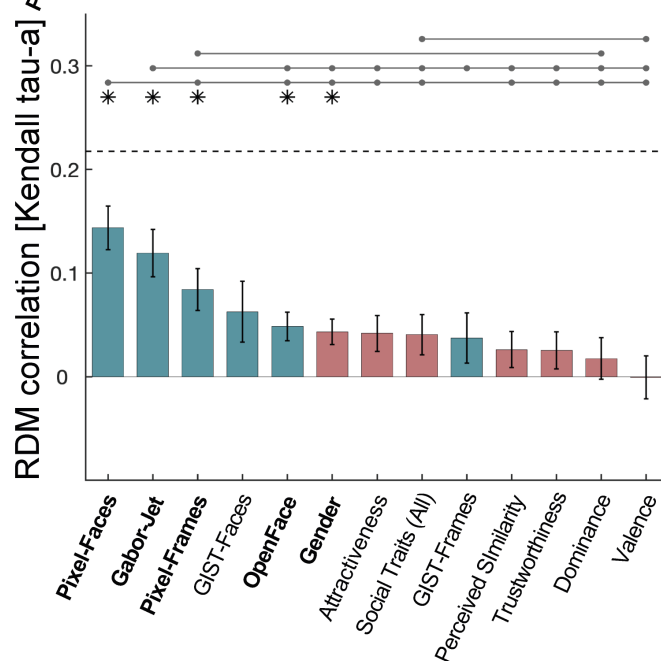
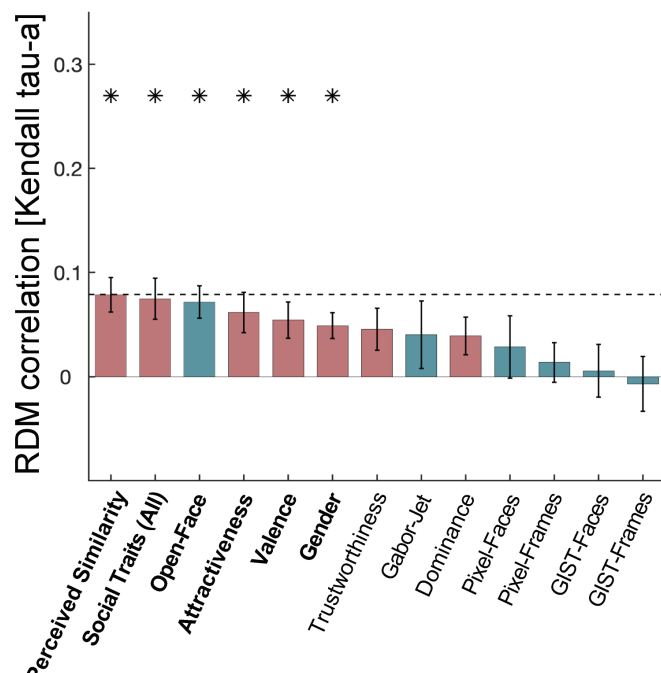
rOFA



rpSTS



B. Kendall tau-a

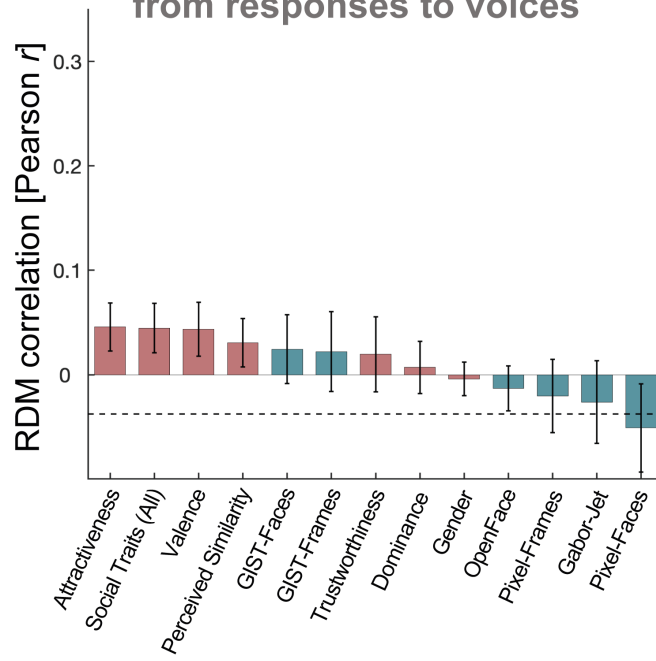


Perceived-property models

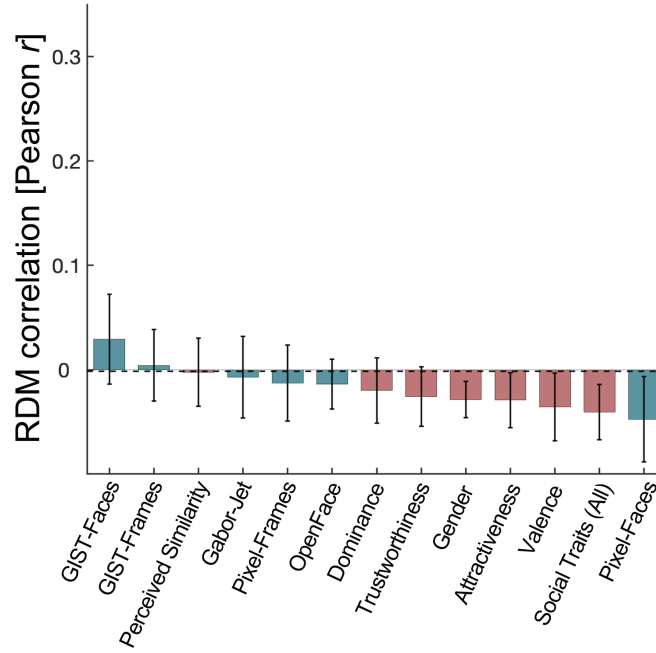
Image-computable models

Brain RDMs computed from responses to voices

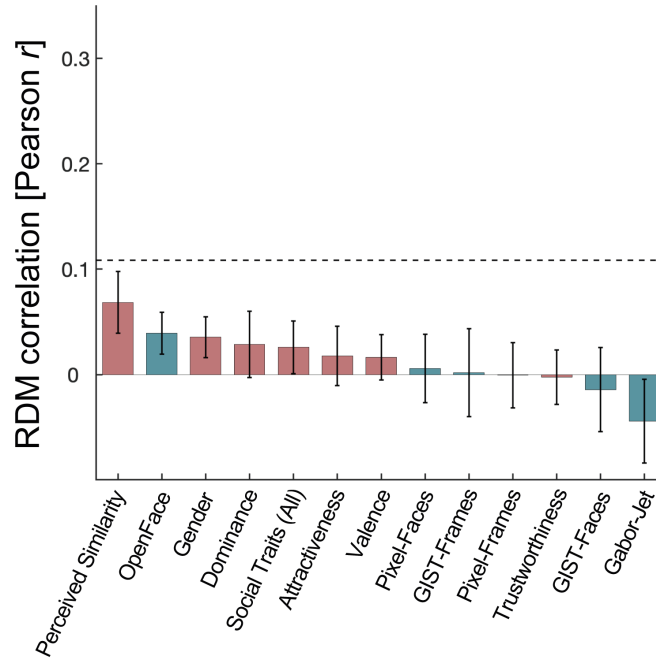
rFFA



rOFA



rpSTS



Perceived-property models Image-computable models

FFA and OFA encode distinct types of face identity information

— Extended data

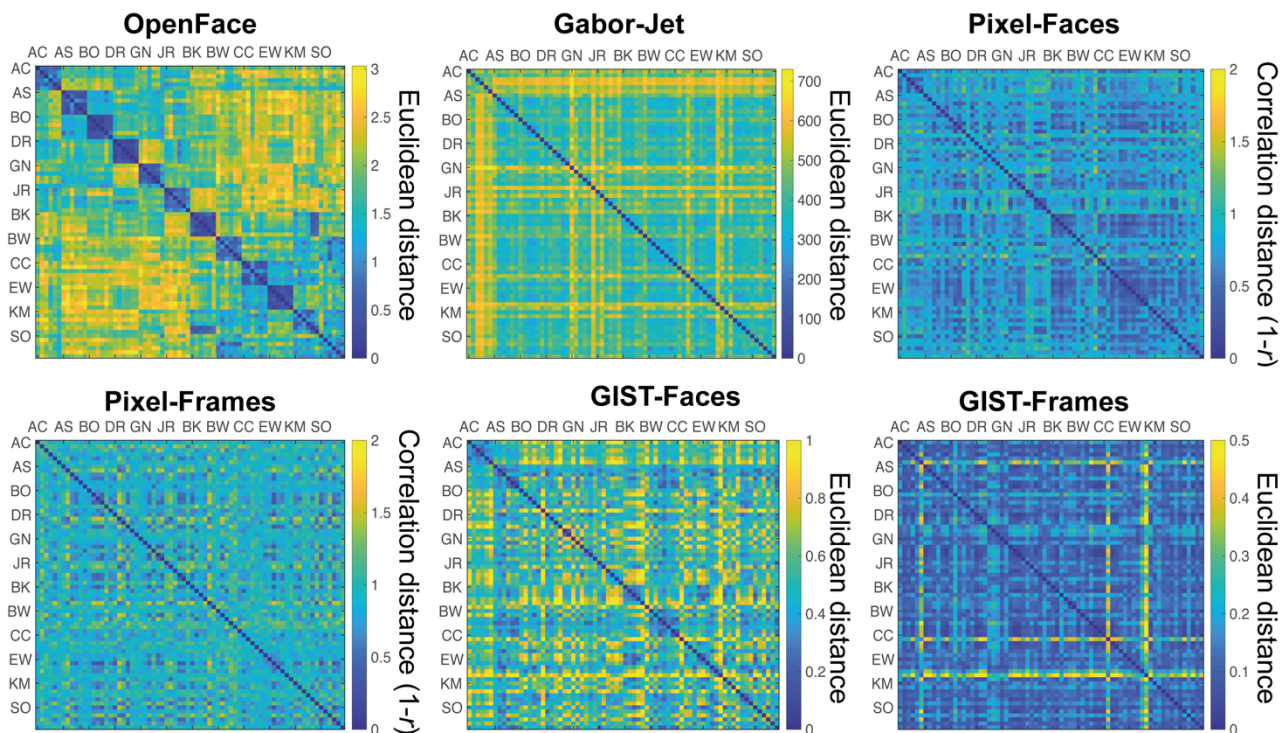


Figure 2-1. Image-computable model representational dissimilarity matrices (RDMs) per image. Model RDMs computed from dissimilarities between images for OpenFace, Gabor-Jet, Pixel-Faces, Pixel-Frames, GIST-Faces, and GIST-Frames. Each row/column represents a single image, and images are clustered by identity (6 images for each of the 12 identities). Each cell shows the dissimilarity between the two images in the corresponding rows and columns, with a value of zero indicating that images are identical. Matrices are symmetric around a diagonal of zeros. From these models, only the OpenFace model grouped different images of the same identity as more similar compared to images from different identities. [Please note that these full RDMs were not used in any analysis. Instead, we created 12x12 RDMs \(one entry for each of the 12 identities\) to be comparable to the brain RDMs \(Figure 2C\). To create the 12x12 RDMs, we computed the mean of all cells that showed images of the same identity pair.](#)

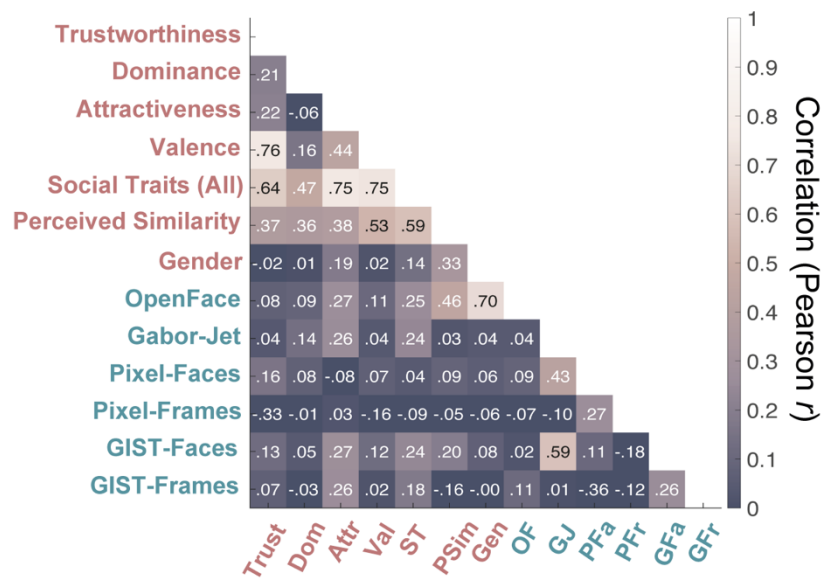


Figure 2-2. Correlations (Pearson) between the different model RDMs. The different candidate models were compared with each other using Pearson correlation. This is the same figure as 2D, but with added correlation values for each cell.